We suggest that exogenically triggered global thermal segregation of bright and dark material on Iapetus is a likely explanation for both the extreme amplitude and the shape of Iapetus' albedo dichotomy. In our model, the uniqueness of Iapetus is attributable not so much to a unique exogenic darkening mechanism (because the initial darkening may be relatively modest) than to a unique combination of size, heliocentric distance, and rotation rate, which allows global migration of the water ice in response to the exogenic darkening.

References and Notes

1. J. D. Cassini, *Philos. Trans. R. Soc.* **12**, 831 (1677).
2. B. A. Smith *et al.*, *Science* **215**, 504 (1982).
3. S. W. Squyres, C. Sagan, *Nature* **303**, 782 (1983).
4. R. A. J. Matthews, *Q. J. R. Astron. Soc.* **33**, 253 (1992).
5. S. Marchi, C. Barbieri, A. Dell'Oro, P. Paolicci, *Astron. Astrophys.* **381**, 1059 (2002).
6. R. G. Tabak, W. M. Young, *Earth Moon Planets* **44**, 251 (1989).
7. T. Denk, G. Neukum, *Lunar Planet. Sci. Conf.* **XXXI**, abstr. 1660 (2000).
8. T. C. Owen *et al.*, *Icarus* **149**, 160 (2001).
9. S. Soter, paper presented at the IAU Colloquium 28, Cornell University, Ithaca, NY, 18 to 21 August 1974.
10. J. A. Burns, D. P. Hamilton, F. Mignard, S. Soter, in *Physics, Chemistry, and Dynamics of Interplanetary Dust*, ASP Conference Series 104, B. Å. S. Gustafson, M. S. Hanner, Eds. (Astronomical Society of the Pacific, San Francisco, 1996), pp. 179–182.
11. B. J. Buratti, M. D. Hicks, K. A. Tryka, M. S. Sittig, R. L. Newburn, *Icarus* **155**, 375 (2002).
12. A. F. Cook, F. A. Franklin, *Icarus* **13**, 282 (1970).
13. P. D. Wilson, C. Sagan, *Icarus* **122**, 92 (1996).
14. D. P. Cruikshank *et al.*, *Icarus* **53**, 90 (1983).
15. J. F. Bell, D. P. Cruikshank, M. J. Gaffey, *Icarus* **61**, 192 (1985).
16. B. J. Buratti, J. A. Mosher, *Icarus* **115**, 219 (1995).
17. C. Peterson, *Icarus* **24**, 499 (1975).
18. T. Denk *et al.*, *Science* **10**, (2009).
19. D. A. Mendis, W. I. Axford, *Annu. Rev. Earth Planet. Sci.* **2**, 419 (1974).
20. D. A. Mendis, W. I. Axford, *J. Geophys. Res.* **113**, A11217 (2008).
21. F. M. Flasar *et al.*, *Space Sci. Rev.* **115**, 169 (2004).
22. C. J. A. Howett, J. R. Spencer, J. C. Pearl, M. Segura, *Icarus* 10.1016/j.icarus.2009.07.016 (2009).
23. J. R. Spencer, L. A. Lebofsky, M. V. Sykes, *Icarus* **78**, 337 (1989).
24. C. E. Bryson, V. Cazcarra, L. L. Levenson, *J. Chem. Eng. Data* **19**, 107 (1974).
25. D. E. Gault, F. Hoerz, D. E. Brownlee, J. B. Hartung, in *Proceedings of the Fifth Lunar Science Conference* (Pergamon, New York, 1974), vol. 3, pp. 2365–2386.
26. J. Veverka, in *Planetary Satellites*, J. Burns, Ed. (Univ. of Arizona Press, Tucson, AZ, 1977), p. 171–209.
27. B. J. Buratti, J. Veverka, *Icarus* **58**, 254 (1984).
28. B. J. Buratti, J. A. Mosher, *Icarus* **90**, 1 (1991).
29. B. J. Buratti, J. A. Mosher, P. D. Nicholson, C. A. McGhee, R. French, *Icarus* **136**, 223 (1998).
30. D. Morrison, N. D. Morrison, in *Planetary Satellites*, J. Burns, Ed. (Univ. of Arizona Press, Tucson, AZ, 1977), pp. 363–378.
31. See supporting material on *Science* Online.
32. J. R. Spencer, *Icarus* **69**, 297 (1987).
33. L. M. Prockter *et al.*, *Icarus* **135**, 317 (1998).
34. J. M. Moore *et al.*, *Icarus* **140**, 294 (1999).
35. N. G. Purves, C. B. Pilcher, *Icarus* **43**, 51 (1980).
36. C. C. Porco *et al.*, *Science* **307**, 1237 (2005).
37. A. R. Hendrix, C. J. Hansen, *Icarus* **193**, 344 (2008).
38. D. P. Cruikshank *et al.*, *Icarus* **193**, 334 (2008).
39. S. J. Ostro *et al.*, *Icarus* **183**, 479 (2006).
40. G. J. Black, D. B. Campbell, L. M. Carter, S. J. Ostro, *Science* **304**, 553 (2004).
41. T. Roatsch *et al.*, *Planet. Space Sci.* **57**, 83 (2009).
42. F. M. Flasar *et al.*, *Science* **307**, 1247 (2005).
43. S. Albers, http://laps.noaa.gov/albers/sos/saturn/iapetus/iapetus_rgb_cyl_www.jpg (2008).

44. We dedicate this paper to the late Steve Ostro, for his invaluable insights into the subsurface structure of Iapetus. We acknowledge the magnificent work by the Cassini project that made possible the observations presented here, and in particular the work of J. Pearl, M. Segura, and other members of the Cassini CIRS team. Supported by the Cassini project and by NASA grants NNX07AU40G and NNG04GK67G, and by the German Aerospace Center (DLR).

Supporting Online Material

www.sciencemag.org/cgi/content/full/science.1177132/DC1
SOM Text
Figs. S1 to S4
Table S1
References

1 June 2009; accepted 3 December 2009
Published online 10 December 2009;
10.1126/science.1177132
Include this information when citing this paper.

Iapetus: Unique Surface Properties and a Global Color Dichotomy from Cassini Imaging

Tilmann Denk,[1]* Gerhard Neukum,[1] Thomas Roatsch,[2] Carolyn C. Porco,[3] Joseph A. Burns,[4] Götz G. Galuba,[1] Nico Schmedemann,[1] Paul Helfenstein,[4] Peter C. Thomas,[4] Roland J. Wagner,[2] Robert A. West[5]

Since 2004, Saturn's moon Iapetus has been observed repeatedly with the Imaging Science Subsystem of the Cassini spacecraft. The images show numerous impact craters down to the resolution limit of ~10 meters per pixel. Small, bright craters within the dark hemisphere indicate a dark blanket thickness on the order of meters or less. Dark, equator-facing and bright, poleward-facing crater walls suggest temperature-driven water-ice sublimation as the process responsible for local albedo patterns. Imaging data also reveal a global color dichotomy, wherein both dark and bright materials on the leading side have a substantially redder color than the respective trailing-side materials. This global pattern indicates an exogenic origin for the redder leading-side parts and suggests that the global color dichotomy initiated the thermal formation of the global albedo dichotomy.

Since 2004, the Imaging Science Subsystem (ISS) (*1*) onboard the Cassini spacecraft has observed the saturnian moon Iapetus (Fig. 1 and table S1) during multiple campaigns (table S2), including a close, targeted flyby on 10 September 2007 (*2*). One reason for Iapetus being a primary target for the Cassini instruments was its unique global albedo dichotomy (*3*), the first surface property ever detected on a planetary moon outside the Earth-Moon system. The roughly elliptical, very dark area on the leading hemisphere (named Cassini Regio) has been repeatedly observed by Cassini ISS; it covers ~40% of the surface and is precisely centered at the middle of Iapetus' leading side at 0°N, 93.5°W (*4*). Cassini Regio is found to be homogeneously dark, with two exceptions: small, bright craters deep within the dark terrain and bright, mainly poleward-facing slopes closer to the edges.

We have identified brighter-than-average craters with diameters up to ~200 m within the highest-resolution images; they display features ranging from subtly lightened rims to obvious bright floors and bright-ray systems. The brightest one, Escremiz (Fig. 2, A and B), is about four times brighter than its surroundings. Only a few percent of these craters are more than twice as reflective as their environs, whereas all others have almost faded to the average albedo of Cassini Regio.

If the darkening process is uniform for all fresh craters, then the brightest craters should be the youngest. With this concept as a guide, we roughly estimated when different craters were formed (*5*). Figure 2C shows that fresh craters fade very quickly. If a new crater has excavated icy material that is ~10 times brighter than the dark Cassini Regio coating (and, thus, about as bright as icy parts of the trailing side), it is only about half as bright ~10,000 years later. After ~10 million years, it has faded to approximately half of the brightness of the surrounding dark terrain. Extrapolating these data from the observed area to the whole Cassini Regio indicates that the largest bright-ray crater with an age similar to Escremiz should be ~200 m in size and that slightly more than 100 craters similar or larger in size and comparable or younger in age than Escremiz should exist on Iapetus' dark hemisphere.

[1]Institut für Geologische Wissenschaften, Freie Universität Berlin, 12249 Berlin, Germany. [2]Institut für Planetenforschung, Deutsches Zentrum für Luft- und Raumfahrt (DLR), Rutherfordstraße 2, 12489 Berlin, Germany. [3]Cassini Imaging Central Laboratory for Operations (CICLOPS), Space Science Institute, 4750 Walnut Street, Suite 205, Boulder, CO 80301, USA. [4]Department of Astronomy, Cornell University, Space Sciences Building, Ithaca, NY 14853, USA. [5]Jet Propulsion Laboratory (JPL), California Institute of Technology, 4800 Oak Grove Drive, Pasadena, CA 91109, USA.

*To whom correspondence should be addressed. E-mail: Tilmann.Denk@fu-berlin.de

The visual appearance of crater Escremiz implies that the dark material is, at most, a few meters thick. For a diameter of ~60 m, the crater depth should be on the order of ~10 m (*6*). Because Escremiz shows a completely bright crater floor and no indication of layering in the crater walls (Fig. 2B), its dark blanket should be much less thick, consistent with results from radar experiments that estimate thicknesses of only decimeters (*7*, *8*).

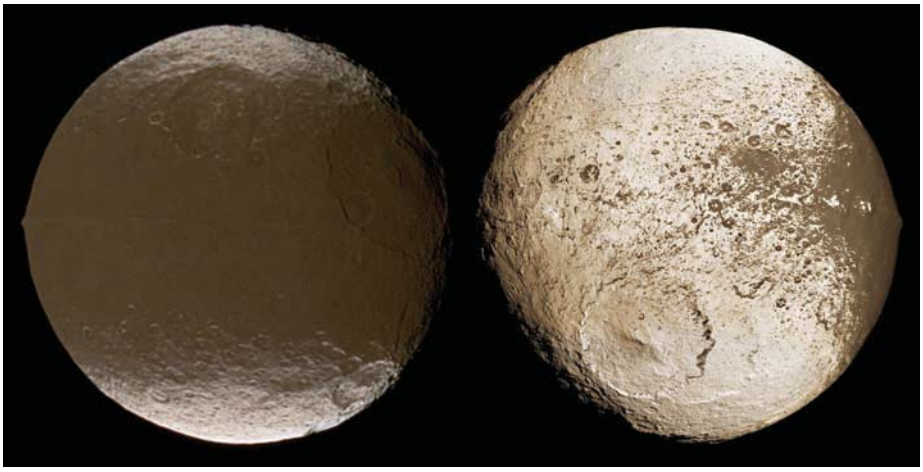

Fig. 1. Global views of Iapetus' dark leading side (**left**) (image IDs: N1482859847 to N1482859953) and its bright trailing side (**right**) (image IDs: N1568157586 to N1568160072); north is up. Turgis (17°N, 28°W), with a diameter of ~580 km, is the largest known well-preserved basin on Iapetus and is visible in the dark Cassini Regio at its eastern edge. The prominent basin on the southern trailing side (on the lower left side of the right-hand plot) is Engelier (41°S, 265°W, ~504 km).

The other exceptions to the observed homogeneity of Cassini Regio are bright, poleward-facing crater walls at mid-latitudes and near the eastern and western boundaries. Above ~28° latitude north or south on Iapetus' leading side, still inside but near the northern or southern edge of Cassini Regio, the observed craters are dark, but the majority of their poleward-facing rims and central peaks is bright and presumably icy (Fig. 1, left, and fig. S1). The strong correlation of the appearance of local dark/bright patches to their planetographic latitude and slope direction suggests that they were formed through runaway temperature-driven water-ice sublimation (*9*). Whereas areas of lower solar irradiation remain bright, areas of higher irradiation lose their water-ice component, leaving behind the more refractory dark component.

The visual appearance of bright craters with dark, equator-facing walls above ~45° latitude, just outside Cassini Regio (again on the leading side) (fig. S1) (*10*), is also a strong indication that this temperature-dependent effect takes place. Another possible interpretation, in which these dark slopes result from exogenically infalling material, appears unlikely. In this case, the orientation of the dark

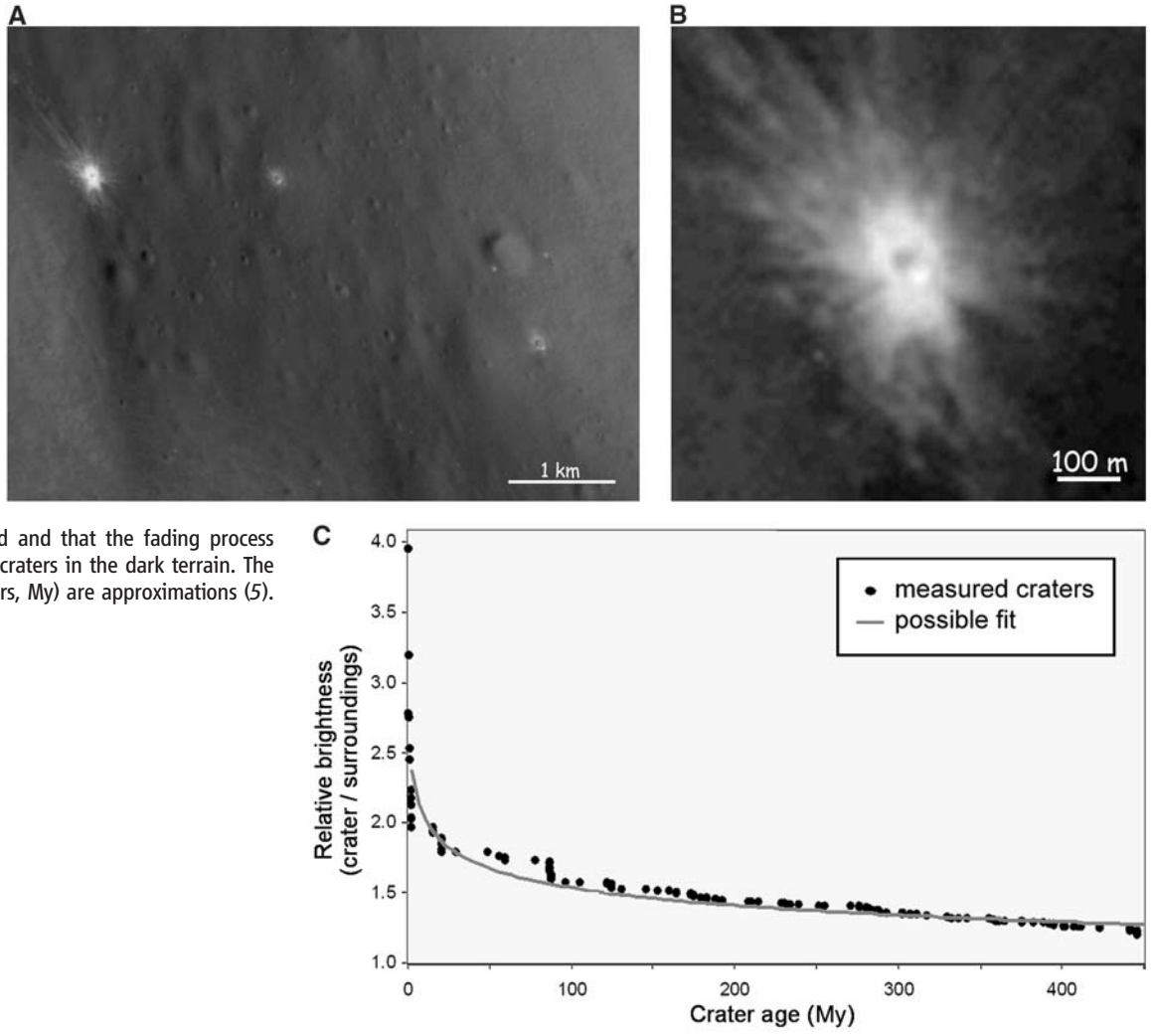

Fig. 2. (**A**) Bright craters within the dark terrain, observed during closest approach of the targeted flyby. Bright-ray crater Escremiz (1.6°N, 173.5°W, diameter ~60 m; at the upper left) is the most prominent of the observed craters of this class on Iapetus. Image ID: N1568127660. (**B**) Enlarged and contrast-enhanced display of Escremiz. (**C**) Brightnesses of small craters within the dark terrain versus individual crater age, under the assumption that brightness and age are directly correlated and that the fading process acts similarly on all fresh craters in the dark terrain. The crater ages (in million years, My) are approximations (*5*).

slopes would be point-symmetric about the center of Iapetus' leading side (the apex of motion) and not mirror-symmetric with respect to the equator, as observed by the Cassini camera.

A common property of these local dark/bright variations is sharp albedo boundaries (at pixel scales of several tens to hundreds of meters), both inside and outside Cassini Regio. Discrete dark patches are even observed on the trailing side, far away from Cassini Regio. Near the equator (continuing to ~20° north or south latitude), these patches are often correlated with depressions, especially with dark-floored craters and troughs (fig. S2). At latitudes up to ~55°, dark patches are only seen on equator-facing slopes (fig. S3). At higher latitudes, no dark spot has been imaged on the trailing side.

Besides very small craters and craters with distinct albedo patterns, a large number of regular impact craters of all sizes have shaped Iapetus' landscape. The generally high crater density indicates that both the bright and the dark surface areas of Iapetus are globally ancient. At large sizes, we find old, often degraded basins with diameters nearly reaching Iapetus' radius (*11*). No other saturnian moon shows so many large basins. In many areas, craters smaller than ~5 to 10 km follow a –2 power law in the cumulative crater size-frequency diagram, indicating an equilibrium distribution ("crater saturation"). However, there are also regions (for instance, within the large basins) where the smaller-crater frequencies do not lie along the –2 equilibrium distribution. For such terrains, and globally for craters >10 km in size, it is possible to determine the production function (Fig. 3).

Our data also provide clear evidence that earlier hypotheses for the formation of the global albedo dichotomy, postulating infall of interplanetary or circum-saturnian dust as the cause, do not work. The complex mottling that appears along the boundary dividing the albedo dichotomy (fig. S4) prevents all explanations except those involving endogenic geologic activities or thermally driven sublimation processes, as in the thermal-migration model of Spencer and Denk (*12*). However, to function properly, this model requires a small, continuous nonthermal darkening process on the leading side to initiate the longitudinal thermal asymmetry between the low-latitude terrain on the leading and trailing sides.

A global color and brightness pattern, which is apparent in the ISS data and is distinct from the long-known global albedo dichotomy, could provide this required trigger. The spectral slopes of leading-side surface materials are generally steeper and redder than those of trailing-side materials across both bright and dark terrains at near-infrared wavelengths. At near-ultraviolet wavelengths, the dark material of the leading side has flatter spectra than that of the trailing side (Fig. 4). Unlike the more elliptically shaped albedo dichotomy, this color dichotomy is well separated into two simple hemispheres (Fig. 4 and fig. S6). The approximate boundaries near the sub-Saturn and anti-Saturn meridians are gradual over hundreds of kilometers but are nevertheless obvious in the images. They are not correlated with the dark terrain; rather, they subdivide even the otherwise (and colorwise) very homogeneous Cassini Regio into two different hues. Similarly, the bright mid-latitude and polar regions on the leading side are redder and darker than their counterparts on the trailing side (figs. S5 and S6).

This hemispheric color pattern suggests an exogenic origin for the color dichotomy. Although rejected as potential causes for the albedo dichotomy, some of the previously proposed hypotheses for the origin of the albedo dichotomy (via ballistic mechanisms) might actually explain the color dichotomy. We reconsider three options: (i) direct impact by interplanetary micrometeoroids (*13*, *14*), (ii) the continuous inflow of reddish dust that originates from the outer saturnian irregular satellites after they are struck by the interplanetary flux (including macroscopic impacts) (*15*–*19*), and (iii) collisions with ejecta formed during a one-time violent impact on Iapetus or another nearby moon (*20*). The dust in process (i) reaches Iapetus on interplanetary paths, whereas that from processes (ii) and (iii) travels on circumsaturnian orbits. Processes (i) and (ii) would be long-term or ongoing, whereas (iii) would probably have happened early in the history of the solar system.

Saturn's ability to gravitationally focus interplanetary material at Iapetus' orbit is modest (*21*). Thus, if interplanetary dust darkened and reddened Iapetus' surface as strongly as in mechanism (i), the irregular saturnian moons should also be reddened substantially at visual wavelengths. However, this is not observed; Phoebe is not red (*18*, *22*). Furthermore, closer to Saturn, the dust flux should increase because of gravitational focusing, either

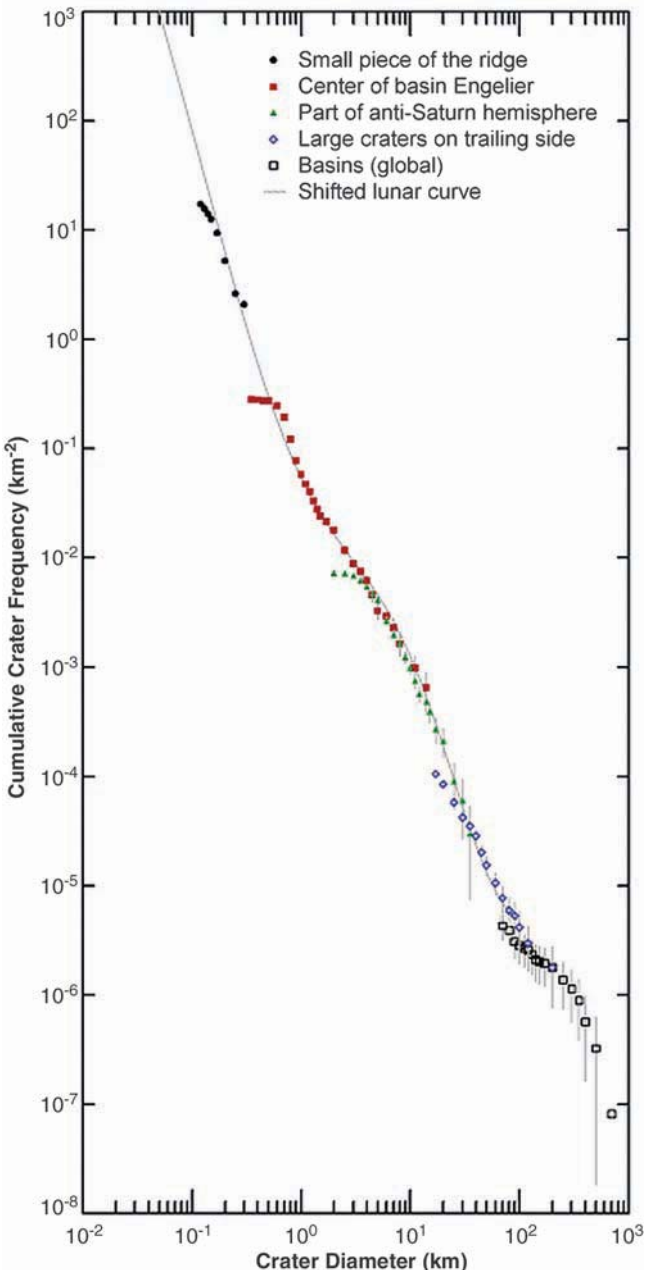

Fig. 3. Cumulative crater size-frequency distribution of Iapetus, combining five individual measurements that are identified by different colors and symbols. Crater sizes of ~300 to ~600 m are missing because no area was observed at sufficient resolution that is young enough to show this part of the production function. Data-point roll-overs at the smaller sizes in each sample occur because of the limited spatial resolution of each of the measured images. The thin line shows the crater size-frequency distribution of Earth's Moon (*40*), shifted by a factor of ~5 toward smaller craters, for comparison. Image IDs from our data: N1568126582, N1568158175, and W1568128142 from the targeted flyby; Iapetus basemap (*41*).

strongly reddening and darkening Mimas' leading side or, alternatively, its trailing side and poles if plasma drag determines the paths of dust within the saturnian magnetosphere (*23*). Again, neither is observed (*24*). Therefore, interplanetary material is not a likely cause of Iapetus' color dichotomy.

An early giant impact [explanation (iii)] that created a debris swarm to later produce the color dichotomy also seems improbable. Cassini images show that Iapetus' leading side is uniformly dark at low latitudes. Without a darkening process that continues at least until the time when the youngest medium-sized crater in Cassini Regio was emplaced, there is no obvious reason why such youthful craters like Malun (fig. S7) should have darkened as well, and Iapetus should exhibit some larger bright-floor and bright-ray craters deep within Cassini Regio. Yet, Cassini images do not show any hints of this.

In hypothesis (ii), impact ejecta lost from the outer satellites must move inward. Solar-radiation pressure and Poynting-Robertson drag have been found to provide plausible mechanisms to spiral in dust along the warped Laplacian plane toward Iapetus' leading side (*16*, *17*, *19*). For the gravity and surface area of an irregular moon, sizes on the order of tens of kilometers might provide the optimal dimensions (*25*). Phoebe (214 km) (*10*) is larger, Ymir (~18 km) is about right, and the other 27 known retrograde irregular moons (estimated sizes of ~4 to 8 km) (*26*) are somewhat undersized. Although the nine known prograde irregular moons (~7 to 40 km) fit better in this size range, they are not candidate sources because impacts of prograde dust on prograde Iapetus occur more or less isotropically with ~0 km/s, whereas impacts of retrograde dust occur head-on into the leading side at ~6.5 km/s and are swept up much more efficiently by Iapetus. The probability of collisions into Iapetus might even increase by more than one order of magnitude for particles coming with inclinations >170° (*19*), and of the dust released from the respective moons, fractions of more than 20% might collide with Iapetus (*17*, *19*). Substantial amounts of retrograde-orbiting debris might also have been produced by collisions of Phoebe and other retrograde moons with several former irregular moons (*27*, *28*). A debris cloud similar to the one that is required for this model to work appears to have recently been found (*29*).

Another argument for hypothesis (ii) is the appearance of chaotically tumbling Hyperion, the next known satellite interior to Iapetus. Its unusual reddish color and intermediate albedo (with respect to dark Cassini Regio and the bright icy surfaces of the other saturnian moons) might be a result of the same process that formed Iapetus' color dichotomy (*30*), whereas Titan fully protects the inner moons from outer dust (*17*). A prediction of this scenario is that synchronously rotating, so far undetected, hypothetical moons outside Titan's orbit should show a global asymmetry as well.

However, issues remain even with this hypothesis. For instance, it is not known if a few particular moons provide the bulk of the dust or if all contribute similarly and if these moons even produce dust of the appropriate color. Furthermore, the colors of these moons are more or less unknown, as are processes such as dust grain-size selection by radiation effects. Other unanswered questions concern the sputtering physics of the dust, how impact-heating alters the dust's color, possible magnetospheric influences on the dust transport (especially near the midnight side of Saturn), and potential grain-size selection processes, but none of these appears insurmountable at first glance.

Callisto (fig. S8), the outermost regular moon of Jupiter, and Neptune's moon, Triton, do not exhibit anything similar to the Iapetus color dichotomy in Voyager or Galileo data (*31*, *32*). Because Callisto is located deep within the jovian magnetosphere and Triton possesses a thin atmosphere, their situations are very different from Iapetus'. The two atmosphereless regular moons orbiting permanently or temporarily outside the magnetosphere of Uranus are a better comparison. Indeed, Oberon and Titania revealed substantially redder leading versus trailing sides in Voyager 2 images, whereas the inner moons Umbriel, Ariel, and Miranda did not (*33*). It is plausible to assume that retrograde dust (with respect to the planetocentric system) from the outer Uranian moons coated the leading sides of those moons that are temporarily or permanently orbiting outside the magnetosphere, similar to the formation of the color dichotomy on Iapetus and the reddening of Hyperion in the saturnian system. This comparison also suggests that dust and debris from outer moons is the most likely cause of the color dichotomy on Iapetus.

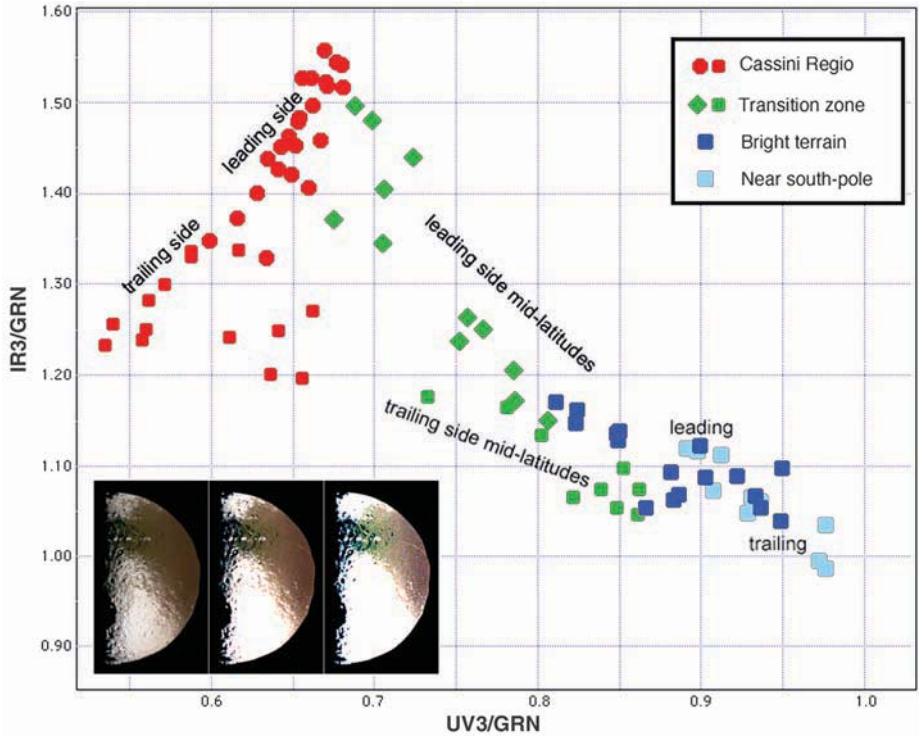

Fig. 4. Color-ratio diagram for parts of the anti-Saturn hemisphere of Iapetus, showing the colors of the leading and trailing sides. Each dot represents a slope of a three-color spectrum in a particular, randomly selected location. The left axis displays the long-wavelength ratio [color ratio between images taken in the 953 nm (IR3) and 563 nm (GRN) filters]; the horizontal axis gives the short-wavelength slopes [color ratio between images taken in the 340 nm (UV3) and GRN filters] of the spectra. (Inset) Image from which these color slopes have been measured (image IDs: N1476574148, N1476574185, and N1476574238). (**Left**) Normal contrast showing the color differences in the bright terrain; (**center**) enhanced contrast; (**right**) extreme contrast enhancement, indicating the color differences within the dark terrain.

References and Notes

1. C. C. Porco *et al.*, *Space Sci. Rev.* **115**, 363 (2004).
2. www.geoinf.fu-berlin.de/projekte/cassini/cassini_fu_iapetus_flyby.php (2007).
3. J. D. Cassini, *Journal des Sçavans* **1677** (issue no. VI), 70 (1677).
4. The mean location of the center of Iapetus' leading side (the hemisphere facing the direction of Iapetus' motion) is not at 90.0°W longitude, but rather at 93.5°W because the surface coordinate system is defined so as to place the crater Almeric at 276.0°W (*34*).
5. See supporting material on *Science* Online for a detailed description of the age estimations.
6. C. R. Chapman, W. B. McKinnon, in *Satellites*, J. A. Burns, M. S. Matthews, Eds. (Univ. of Arizona Press, Tucson, AZ, 1986), pp. 492–580.
7. G. J. Black, D. B. Campbell, L. M. Carter, S. J. Ostro, *Science* **304**, 553 (2004).
8. S. J. Ostro *et al.*, *Icarus* **183**, 479 (2006).
9. J. R. Spencer, *Icarus* **69**, 297 (1987).
10. C. C. Porco *et al.*, *Science* **307**, 1237 (2005).
11. B. Giese *et al.*, *Icarus* **193**, 359 (2008).
12. J. R. Spencer, T. Denk, *Science* **327**, 432 (2010); published online 10 December 2009 (10.1126/science.1177132).
13. A. F. Cook, F. A. Franklin, *Icarus* **13**, 282 (1970).
14. P. D. Wilson, C. Sagan, *Icarus* **122**, 92 (1996).
15. S. Soter, paper presented at the IAU Colloquium 28, Cornell University, Ithaca, NY, 18 to 21 August 1974.

16. J. A. Burns, P. L. Lamy, S. Soter, *Icarus* **40**, 1 (1979).
17. J. A. Burns, D. P. Hamilton, F. Mignard, S. Soter, in *Physics, Chemistry, and Dynamics of Interplanetary Dust*, ASP Conference Series 104, B. Å. S. Gustafson, M. S. Hanner, Eds. (Astronomical Society of the Pacific, San Francisco, 1996), pp. 179–182.
18. B. J. Buratti, M. D. Hicks, K. A. Tryka, M. S. Sittig, R. L. Newburn, *Icarus* **155**, 375 (2002).
19. F. Tosi *et al.*, preprint available at http://arxiv.org/abs/0902.3591 (2009).
20. Besides Iapetus, Hyperion, Titan, and outer-satellite impacts were suggested; see also (*12*).
21. Reference (*18*) mentions an increase of the dust flux by ~20%, whereas (*35*) finds as much as a factor of 3 for some cases.
22. D. J. Tholen, B. Zellner, *Icarus* **53**, 341 (1983).
23. The leading sides of the moons beyond Mimas and inside Titan should be substantially coated by E-ring particles (*24*, *36*, *37*), making them less useful for this argument.
24. B. J. Buratti, J. A. Mosher, T. V. Johnson, *Icarus* **87**, 339 (1990).
25. J. A. Burns *et al.*, *Science* **284**, 1146 (1999).
26. S. S. Sheppard, www.dtm.ciw.edu/users/sheppard/satellites/satsatdata.html (2009).
27. D. Nesvorný, J. L. A. Alvarellos, L. Dones, H. F. Levison, *Astron. J.* **126**, 398 (2003).
28. D. Turrini, F. Marzari, H. Beust, *Mon. Not. R. Astron. Soc.* **391**, 1029 (2008).
29. A. J. Verbiscer, M. F. Skrutskie, D. P. Hamilton, *Nature* **461**, 1098 (2009).
30. This idea was developed in several papers (*18*, *38*, *39*), but under the assumption that dust from the outer saturnian moons formed Iapetus' albedo dichotomy.
31. T. V. Johnson *et al.*, *J. Geophys. Res. Solid Earth* **88**, 5789 (1983).
32. T. Denk, R. Jaumann, G. Neukum, in *Lisbon Euroconference Jupiter After Galileo and Cassini, Abstracts Book* 17 to 21 June 2002, Lisbon, Portugal, abstr. no. P-4.1.18, 2002, p. 118.
33. B. J. Buratti, J. A. Mosher, *Icarus* **90**, 1 (1991).
34. M. E. Davies, F. Y. Katayama, *Icarus* **59**, 199 (1984).
35. K. J. Zahnle, P. Schenk, H. Levison, L. Dones, *Icarus* **163**, 263 (2003).
36. K. D. Pang, C. C. Voge, J. W. Rhoads, J. M. Ajello, *J. Geophys. Res. Solid Earth* **89**, 9459 (1984).
37. D. P. Hamilton, J. A. Burns, *Science* **264**, 550 (1994).
38. P. C. Thomas, J. Veverka, *Icarus* **64**, 414 (1985).
39. K. S. Jarvis, F. Vilas, S. M. Larson, M. J. Gaffey, *Icarus* **146**, 125 (2000).
40. G. Neukum, B. A. Ivanov, in *Hazards Due to Comets and Asteroids*, T. Gehrels, Ed. (Univ. of Arizona Press, Tucson, AZ, 1994), pp. 359–416.
41. T. Roatsch *et al.*, *Planet. Space Sci.* **57**, 83 (2009).
42. We acknowledge the individuals at CICLOPS (at the Space Science Institute in Boulder, CO) and JPL (Pasadena, CA), as well as the members and associates of the Imaging Team for the successful conduct of the ISS experiment onboard the Cassini spacecraft. This paper is dedicated to Steve Ostro, whose work helped considerably to explain the nature of Iapetus' dark terrain. This work has been funded by the German Aerospace Center (DLR) and NASA/JPL.

Supporting Online Material

www.sciencemag.org/cgi/content/full/science.1177088/DC1
SOM Text
Figs. S1 to S8
Tables S1 and S2
References and Notes

1 June 2009; accepted 1 December 2009
Published online 10 December 2009;
10.1126/science.1177088
Include this information when citing this paper.

Rules for Biologically Inspired Adaptive Network Design

Atsushi Tero,[1,2] Seiji Takagi,[1] Tetsu Saigusa,[3] Kentaro Ito,[1] Dan P. Bebber,[4] Mark D. Fricker,[4] Kenji Yumiki,[5] Ryo Kobayashi,[5,6] Toshiyuki Nakagaki[1,6]*

Transport networks are ubiquitous in both social and biological systems. Robust network performance involves a complex trade-off involving cost, transport efficiency, and fault tolerance. Biological networks have been honed by many cycles of evolutionary selection pressure and are likely to yield reasonable solutions to such combinatorial optimization problems. Furthermore, they develop without centralized control and may represent a readily scalable solution for growing networks in general. We show that the slime mold *Physarum polycephalum* forms networks with comparable efficiency, fault tolerance, and cost to those of real-world infrastructure networks—in this case, the Tokyo rail system. The core mechanisms needed for adaptive network formation can be captured in a biologically inspired mathematical model that may be useful to guide network construction in other domains.

Transport networks are a critical part of the infrastructure needed to operate a modern industrial society and facilitate efficient movement of people, resources, energy, and information. Despite their importance, most networks have emerged without clear global design principles and are constrained by the priorities imposed at their initiation. Thus, the main motivation historically was to achieve high transport efficiency at reasonable cost, but with correspondingly less emphasis on making systems tolerant to interruption or failure. Introducing robustness inevitably requires additional redundant pathways that are not cost-effective in the short term. In recent years, the spectacular failure of key infrastructure such as power grids (*1*, *2*), financial systems (*3*, *4*), airline baggage-handling systems (*5*), and railway networks (*6*), as well as the predicted vulnerability of systems such as information networks (*7*) or supply networks (*8*) to attack, have highlighted the need to develop networks with greater intrinsic resilience.

Some organisms grow in the form of an interconnected network as part of their normal foraging strategy to discover and exploit new resources (*9*–*12*). Such systems continuously adapt to their environment and must balance the cost of producing an efficient network with the consequences of even limited failure in a competitive world. Unlike anthropogenic infrastructure systems, these biological networks have been subjected to successive rounds of evolutionary selection and are likely to have reached a point at which cost, efficiency, and resilience are appropriately balanced. Drawing inspiration from biology has led to useful approaches to problem-solving such as neural networks, genetic algorithms, and efficient search routines developed from ant colony optimization algorithms (*13*). We exploited the slime mold *Physarum polycephalum* to develop a biologically inspired model for adaptive network development.

Physarum is a large, single-celled amoeboid organism that forages for patchily distributed food sources. The individual plasmodium initially explores with a relatively contiguous foraging margin to maximize the area searched. However, behind the margin, this is resolved into a tubular network linking the discovered food sources through direct connections, additional intermediate junctions (Steiner points) that reduce the overall length of the connecting network, and the formation of occasional cross-links that improve overall transport efficiency and resilience (*11*, *12*). The growth of the plasmodium is influenced by the characteristics of the substrate (*14*) and can be constrained by physical barriers (*15*) or influenced by the light regime (*16*), facilitating experimental investigation of the rules underlying network formation. Thus, for example, *Physarum* can find the shortest path through a maze (*15*–*17*) or connect different arrays of food sources in an efficient manner with low total length (TL) yet short average minimum distance (MD) between pairs of food sources (FSs), with a high degree of fault tolerance (FT) to accidental disconnection (*11*, *18*, *19*). Capturing the essence of this system in simple rules might be useful in guiding the development of decentralized networks in other domains.

We observed *Physarum* connecting a template of 36 FSs that represented geographical locations of cities in the Tokyo area, and compared the result with the actual rail network in Japan. The *Physarum* plasmodium was allowed to grow from Tokyo and initially filled much of the available land space, but then concentrated on FSs by thinning out the network to leave a subset of larger, interconnecting tubes (Fig. 1). An alternative protocol, in which the plasmodium was allowed to extend fully in the available space and the FSs were then presented simultaneously, yielded similar results. To complete the network formation, we allowed any excess volume of plasmodium to

[1]Research Institute for Electronic Science, Hokkaido University, Sapporo 060-0812, Japan. [2]PRESTO, JST, 4-1-8 Honcho, Kawaguchi, Saitama, Japan. [3]Graduate School of Engineering, Hokkaido University, Sapporo 060-8628, Japan. [4]Department of Plant Sciences, University of Oxford, Oxford OX1 3RB, UK. [5]Department of Mathematical and Life Sciences, Hiroshima University, Higashi-Hiroshima 739-8526, Japan. [6]JST, CREST, 5 Sanbancho, Chiyoda-ku, Tokyo, 102-0075, Japan.

*To whom correspondence should be addressed. E-mail: nakagaki@es.hokudai.ac.jp

www.sciencemag.org/cgi/content/full/1177132/DC1

Supporting Online Material for

Formation of Iapetus' Extreme Albedo Dichotomy by Exogenically Triggered Thermal Ice Migration

John R. Spencer* and Tilmann Denk

*To whom correspondence should be addressed. E-mail: spencer@boulder.swri.edu

Published 10 December 2009 on *Science* Express
DOI: 10.1126/science.1177132

This PDF file includes:

Description of the Numerical Frost Migration Model

Model Concept

The interplay between exogenic darkening, thermal frost migration, and impact gardening on a multi-component planetary surface is undoubtedly very complex. Sublimation is likely to affect small-scale surface morphology in complex ways, (e.g., the formation of penitentes on terrestrial snowfields (*SI*)), and the surface morphology in turn is likely to control the distribution of ice and non-ice components in ways that we cannot predict. Impact gardening is likely to affect ice and non-ice components differently, resulting in different grain morphologies, sizes, and distributions for each component, which will affect the interaction of light with the surface, and thus its albedo. It is thus impossible to model the interplay of these processes with any degree of realism.

However, some qualitative predictions can be made with confidence. It is very likely, for instance, that icy surfaces will darken with the addition of dark material, and will brighten with condensation of ice. Loss of ice from an icy surface that includes some dark material will probably concentrate dark material near the surface, and will thus darken that surface. The surface will be re-mixed by impact gardening or other processes. When sufficient dark material has accumulated on the surface, ice sublimation is likely to be inhibited, both due to formation of a physical barrier to sublimating ice, and to the insulation of the underlying ice from peak daytime temperatures. The presence of apparent local thermally-controlled segregation of bright and dark materials on Iapetus

(*S2*) suggests that these sublimation and darkening processes do in fact occur at geologically-significant rates on Iapetus.

The goal of our model is to capture the essence of these processes with the minimum possible number of free parameters, and with very simple formulations for surface mixing and albedo (equations S1, S2, and S3) which behave in qualitatively plausible ways. Because of the complexity of the processes involved, we do not claim that the model parameters that produce the best fit to Iapetus necessarily correspond to their real-world values. However the fact that we can produce a surface remarkably similar to the real appearance of Iapetus with a very simple model and suitable choices of only a few model parameters, and with a variety of formulations for mixing and albedo, gives us confidence that our model does indeed capture the essential processes responsible for Iapetus' remarkable appearance.

Relationship Between Deposition, Sublimation, and Surface Dark Material Fraction

The greatest simplification in our model involves the determination of the surface fractional abundance of dark material (which controls the surface albedo, temperature, and ice sublimation rate) as a function of the surface's previous history of ice sublimation, ice deposition, and accumulation of exogenic and intrinsic dark material. Rather than attempt an accurate physical description of these processes we use, in most models, the following simple formulation:

$$f_d = (d/m)\ e^{-c/m} \qquad \text{(S1)}$$

where f_d is the surface fractional abundance of dark material, d is the total thickness of dark material, c is the net ice condensation thickness (which can be positive or negative), and m is a vertical mixing length which describes the mixing of ice and dark material into the subsurface, by micrometeorite gardening or other processes. f_d is capped at 1.0, because addition of dark material to a surface already entirely covered in dark material will not change its characteristics further. d may include both an intrinsic component d_0 which is constant with time, and an exogenic component d_t which increases over time. This formula produces results that are at least qualitatively reasonable: surfaces become more ice-rich as ice condenses and become more ice-poor as ice sublimes or dark material is added. Also, addition of sufficient dark material, or loss of sufficient ice, produces a surface that is effectively ice-free, while the effective surface dark fraction only asymptotically approaches zero as ice is added, simulating the effects of the transparency of ice. See Fig. S1.

To explore the sensitivity of the model results to the mixing model used, we also tried a linear mixing model which treats separately the initial, intrinsic component abundance d_0, and the subsequently-added exogenic component d_t:

$$f_d = (\ d_0(m - c) + d_t\ ) / m \qquad \text{(S2)}$$

Again f_d is capped at 1.0 and in addition, negative values of f_d are set to zero. This formulation is illustrated in Fig. S2.

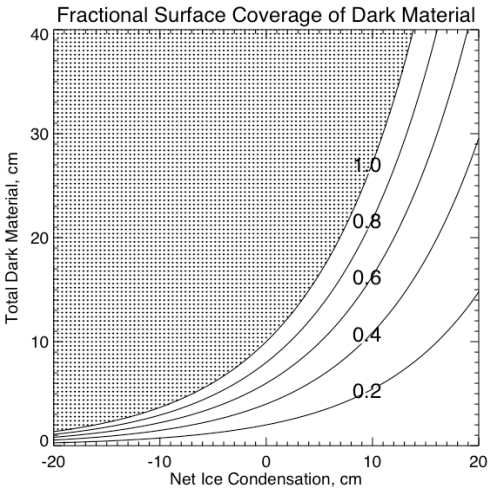

Figure S1 Contour plot of the surface fraction f_d of dark material as a function of ice condensation c and total dark material d, for a mixing length m = 10 cm, using Equation S1. The stippled area indicates the region of parameter space where f_d is capped at 1.0.

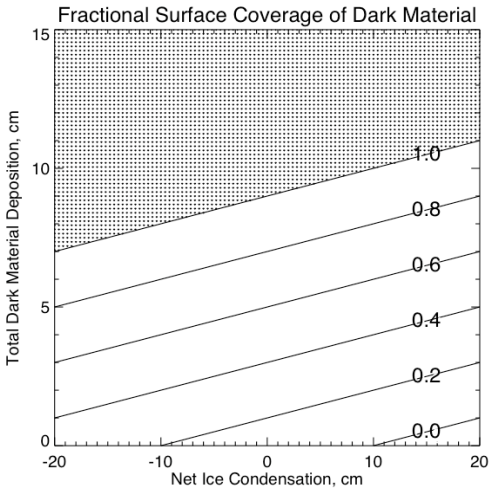

Figure S2 Contour plot of the surface fraction f_d of dark material as a function of ice condensation c and total deposited dark material d_t, for a mixing length m = 10 cm and initial dark fraction d_0 = 0.1, using Equation S2. The stippled area indicates the region of parameter space where f_d is capped at 1.0.

Determination of Surface Albedo

The second simplification involves the determination of surface albedo as a function of the surface fraction of dark material. In reality the albedo of intimately mixed ice and dark material is likely to be a highly non-linear function of dark material abundance (e.g., (*S3*)), but the details of this non-linearity depend on the spatial distribution of the ice and dark material at scales comparable to the path length of individual photons, and cannot be modeled with any accuracy because these parameters are unknown. To simulate the likely non-linearity of the dependence of bolometric albedo A on dark material fraction f_d, we adopt the formulation:

$$A = A_d + (A_i - A_d)\,(1 - f_d)^q \qquad \text{(S3)}$$

where A_i is the albedo of pure ice, A_d is the albedo of pure dark material and q is normally set equal to 2, to account for the fact that a small amount of dark material may have a relatively large effect on albedo. However, we also investigate the effect of using a linear albedo law (q = 1), to simulate the situation where ice and dark material are spatially segregated on scales larger than the photon path length.

Global Ice Migration

In our numerical model, Iapetus is divided into tiles with a latitudinal and longitudinal extent of 2.5°. The surface is assumed to be initially entirely covered in water ice that is uniformly darkened by admixture of a small amount of dark material d_0 intrinsic to Iapetus: this corresponds to the less-red dark component seen by Denk et al. (*S2*). We then add additional exogenic dark material (corresponding to the redder dark component seen on the leading side by Denk et al., though the color of the dark material is irrelevant for our model) at a constant rate $\mathrm{d}d/\mathrm{d}t$ that depends on the angular distance α from the center of the leading hemisphere, to simulate exogenic deposition. We assume a smooth transition of full angular width ϕ from a

peak deposition rate R on the leading hemisphere to zero on the trailing hemisphere, using the functional form

$$\begin{aligned} dd/dt &= R, && \alpha < \theta \\ &= R\,(\cos((\alpha - \theta)\,\pi / (\pi - 2\theta)) + 1) / 2, && \theta < \alpha < \pi - \theta \\ &= 0, && \alpha > \pi - \theta \end{aligned} \qquad \text{(S4)}$$

where $\theta = \pi - \phi / 2$. In most models we assume $\phi = 180°$, so $\theta = 0$ and $dd/dt = R\,(\cos(\alpha) + 1)/2$, but we also explore the effects of changing ϕ below.

At each location on the surface, the annually- and diurnally-averaged upward H_2O sublimation rate is computed from the diurnal and annual variation in temperature, which is in turn computed from albedo and latitude, using a 1-dimensional numerical thermal model (*S4*) assuming a surface thermal inertia of 20 J m^{-2} $s^{-1/2}$ K^{-1}, and including the known annual variation in heliocentric distance, from 9.04 to 10.04 AU, due to Saturn's eccentric orbit. The obliquity of Iapetus, which is time-variable but has an effective value of 15.4°, is not included, and the sun is therefore assumed to be always in the equatorial plane. This simplification will have little effect at low latitudes but will underestimate average sublimation rates within tens of degrees of the poles. As polar sublimation rates are very low compared to those elsewhere on the surface, this simplification is unlikely to affect the model results substantially. Sublimation rates are scaled by the fraction of the surface that is covered in ice, $(1 - f_d)$, so that there is no sublimation from regions entirely covered in a lag deposit of dark material. An exception to this rule is that ice deposited on pure dark material ($f_d = 1$) from elsewhere on the surface in a given timestep is allowed to sublime again in the next timestep, to model the fact that the pure dark material is warmer than the rest of the surface and ice will thus not accumulate there.

The launch directions of molecules subliming from each unit area on the surface are assumed to be distributed uniformly in azimuth and to be distributed in emission angle e (measured from the surface normal) according to $\sin(e)\cos(e)$, which accounts for both the smaller solid angle at small values of e and the foreshortening of each surface element at large values of e (molecules are thus emitted with an angular distribution identical to that of photons scattered from a Lambertian surface). Molecules follow ballistic trajectories which are integrated numerically, accounting for the curvature of the surface and the variation in gravitational acceleration with height, assuming an initial Maxwellian velocity distribution, until they re-impact or escape. Re-impacting molecules are assumed to stick with 100% efficiency. For the purposes of determining molecule speeds and jump distances we assume a single temperature of 115 K to reduce computational complexity: this assumption is justified by the modest dependence of speed and jump distance on temperature. The model ignores the roughly 9% of molecules that escape Iapetus entirely. At 115 K, 6% of molecules jump as far as the antipode or beyond, and the convergence of impacting molecules on the antipode leads to a peak in ice deposition in regions antipodal to regions of maximum sublimation, as is apparent for instance on the trailing hemisphere at 1200 million years in model A in Fig. 3 of the main paper.

Table S1: Model Parameters Used in Fig. S3							
Model	Mixing Length m, cm	Initial Dark Material Abundance d_0/m	Albedo exponent q	Maximum dark material addition rate R, cm/yr	Leading / trailing transition width, ϕ, degrees	Surface Dark Fraction Equation	Comments
A	10	0.16	2	2.5×10^{-9}	180	S1	Fig. 3 in main paper
B	1	0.3	1	3.0×10^{-10}	120	S1	Most "Iapetus-like" model: Fig. 3 in main paper
C	10	0.0	2	2.5×10^{-9}	180	S1	Reduced initial dark abundance
D	10	0.35	2	2.5×10^{-9}	180	S1	Increased initial dark abundance
E	10	0.16	2	2.5×10^{-8}	180	S1	Faster dark material accumulation rate
F	10	0.10	2	2.5×10^{-9}	180	S2	Linear dark fraction model

Sensitivity of Results to Variations in Model Parameters

Different combinations of model parameters produce different results that resemble Iapetus to greater or lesser extent, in varying periods of time. Table S1 lists a range of model parameters, and the resulting final appearances are shown in Fig. S3. All models presented here have A_i = 0.7 and A_d = 0.04.

Models A and B are shown in more detail in Fig. 3 of the main paper. Model A uses a simpler dark material deposition pattern, a mixing length more consistent with likely impact gardening rates, and assumes some intimate mixing of bright and dark materials when determining albedo, while Model B shows how the parameters can be adjusted to most closely match the actual appearance of Iapetus. Reducing the mixing length m to 1 cm, and setting exponent q = 1 (equivalent to assuming small-scale spatial segregation of the ice and dark components) increases the final albedo of mid-latitude ice on the leading hemisphere. In addition, slightly narrowing the angular width ϕ of the transition between maximum and zero dark deposition rates improves the match to the shape of the dark terrain on Iapetus. Given the crudeness of our model, however, these parameters are not necessarily more applicable to Iapetus than the parameters used in other models. This model also exhibits albedo instabilities at low latitudes on the trailing side, possibly analogous to the local thermal segregation also seen on Iapetus in this region. See the discussion below.

Models C and D show the effects of varying the initial dark material abundance d_0. Decreased d_0 increases the time required to acquire an Iapetus-like appearance, and makes the model low-latitude leading hemisphere much brighter than Iapetus, while increased d_0 increases sublimation rates at all longitudes, resulting in an equatorial dark band.

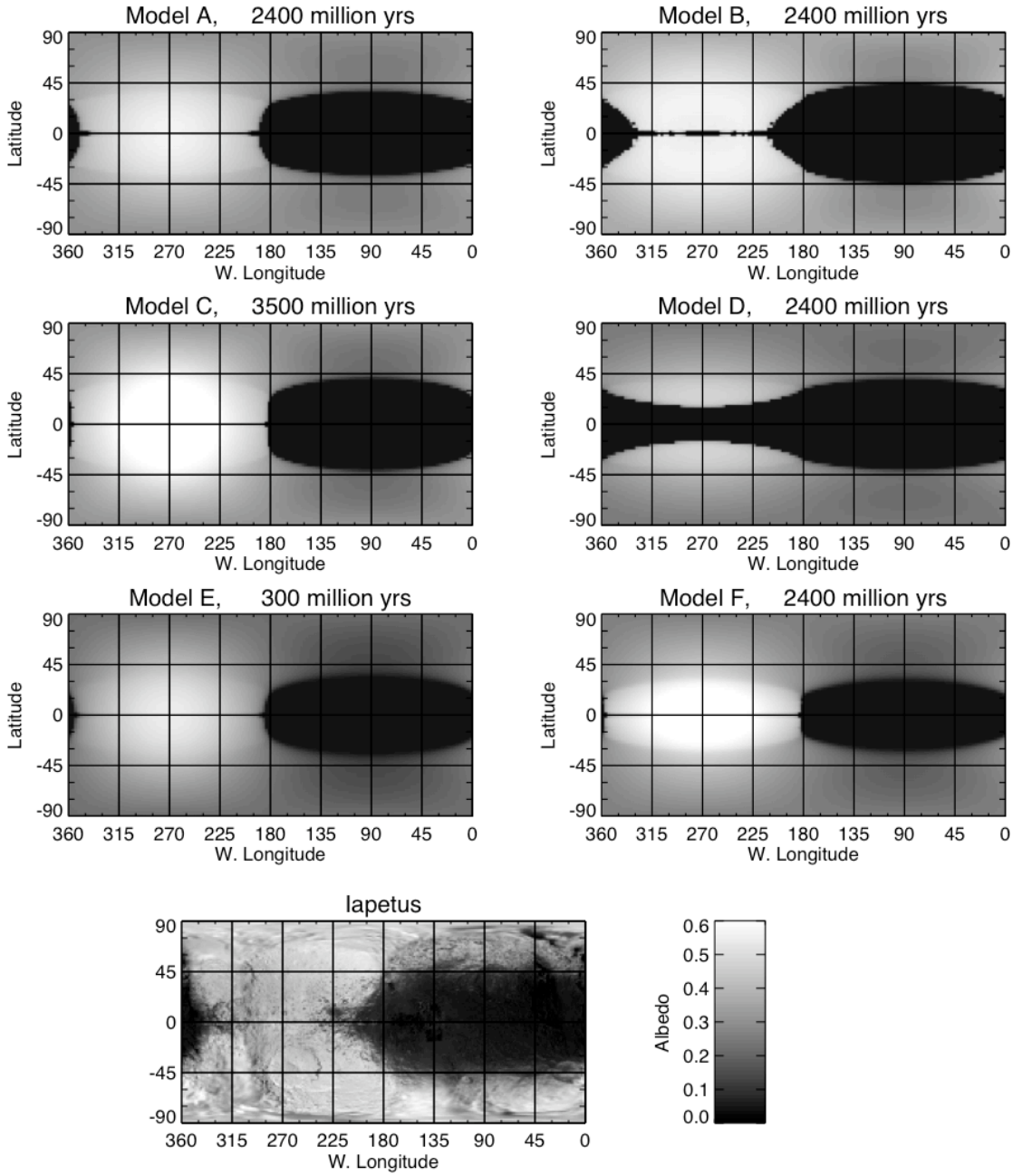

Figure S3 Model albedo patterns resulting from the various model parameters listed in Table S1, compared to the albedo distribution of Iapetus itself (*S5*). All albedo images are scaled as shown by the scale bar, though the Iapetus mosaic is not photometrically accurate, and is scaled very approximately using the bright and dark terrain albedos determined in the main paper from CIRS data.

Model E shows the effects of increasing dark material accumulation rates. For this model, darkening of mid-latitudes on the trailing hemisphere happens more quickly than sublimation can brighten them, resulting in much greater darkening of the entire leading hemisphere than is seen on Iapetus, in just a few hundred million years.

Model F shows the effects of using the mixing law given in equation S2. Overall behavior is not changed dramatically by use of this very different formulation.

In summary, many combinations of parameters and model formulations can produce Iapetus-like results, suggesting that the validity of our model is not critically dependent on the precise details of the model.

Competing Processes

Mass wasting

Mass wasting will compete with sublimation darkening on steep slopes, and it is notable that bright icy surfaces are very rare at low latitudes on Iapetus' dark leading side even on steep slopes (*S2*). These slopes will remain dark provided that resurfacing by mass wasting occurs more slowly than darkening due to the deposition of dark material and the resulting sublimation of ice. As shown in Fig. 2 of the main paper, sublimation rates at low latitudes can be as fast as 10 cm per million years, so it is plausible that sublimation darkening can compete with mass wasting on relatively stable slopes at the angle of repose.

Impact gardening

Impact gardening, which mixes ice and dark material back into the subsurface and thus counteracts albedo changes, is far more complex than assumed in our model. The model uses a single, time-independent, mixing length m, while in actual impact gardening the mixing length is time-dependent. In the Gault et al. lunar regolith mixing model (*S6*), gardening to 0.7 cm depth occurs in ~10^6 years, so the loss of 1 cm of ice could indeed produce a large albedo effect on such timescales. In 10^9 years the Gault model predicts ~10 cm of gardening, so correspondingly larger amounts of sublimation or deposition are required to affect the surface albedo without re-mixing of the dark material into the subsurface. To incorporate a time-dependent mixing length into our model would greatly complicate the model, because the relevant timescale, and thus the relevant mixing length, is not the time since the beginning of the simulation, but the time since the last significant change to the surface. However, by using a constant mixing length our model captures the essential role of impact gardening in mixing accumulated materials into the subsurface.

Low Latitude Albedos on the Trailing Hemisphere

A significant remaining problem with the model predictions concerns the albedo of the ice on the trailing side of Iapetus. Our model predicts that water ice with the observed albedo (~0.39) and temperature (~113 K) of the trailing-side bright terrain should be relatively unstable at low latitudes, and should migrate poleward, leaving a dark lag deposit. However, this does not happen in most of our models (Model D above is an exception), because the low-latitude ice on the trailing hemisphere in the models generally has a final albedo near 0.6, due to deposition of fresh ice. This is substantially higher than observed low-latitude albedos, and is higher than the

albedo of the poles, unlike the slightly brighter polar regions seen in Cassini images of Iapetus' trailing hemisphere (*S2*). Our model's highly-simplified treatment of surface processes may be to blame for this discrepancy. However, we believe that the model's remarkable success in reproducing most other aspects of Iapetus' albedo distribution is strong evidence that it captures the dominant processes responsible for Iapetus' appearance, despite this remaining discrepancy with the observations.

Comparison of Sublimation Rates to Cassini Regio Bright Crater Retention Ages

Denk et al. (*S2*) use the frequency of bright craters to estimate the timescale for complete darkening of these craters to be tens to hundreds of millions of years, depending on the impact flux model used, with initial darkening being much more rapid, perhaps taking less than a million years. Fig. 2B of the main paper shows that for albedos intermediate between the bright and dark terrain on Iapetus, 1 cm of sublimation is possible in a million years, comparable to impact gardening rates in the same period and thus sufficient to cause significant darkening, consistent with our model.

Comparison to Radar Observations

Cassini and ground-based radar observations probe the subsurface of Iapetus and thus provide further tests of our model. Cassini observations at 2.2 cm wavelength show a much higher radar albedo on the optically-bright trailing side than on the dark leading side (*S7*), while 13 cm wavelength ground-based radar observations show a uniformly low albedo on both hemispheres (*S8*). As noted by (*S7)*, these observations suggest that the difference between the two hemispheres is restricted to depths less than the 10s of cm probed by the 13 cm radar, which is consistent with our model in which lag deposits and recondensed ice have thicknesses of cm to 10s of cm, probably controlled by impact gardening depths. The low 13 cm radar albedos may be due to the presence of subsurface NH_3, a strong radar absorber, at depth (*S7*). NH_3 is much more volatile than H_2O, and is likely to be depleted in the uppermost subsurface by both sublimation and impact gardening processes (Fig. S4).

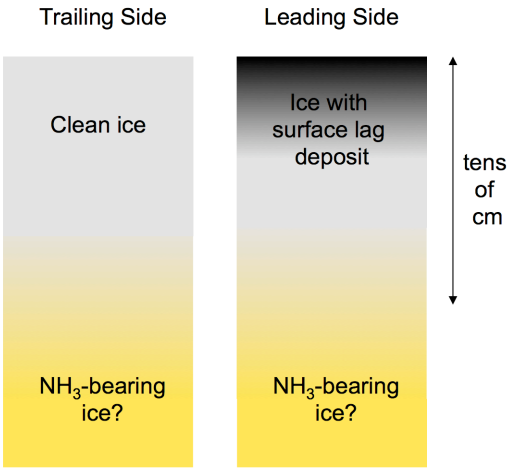

Figure S4 Cartoon of the possible subsurface structure of Iapetus, consistent with our model and based on radar data (*S7*, *S8*).

References

S1. V. Bergeron, C. Berger, M. D. Betterton, *Phys. Rev. Lett.* **96**, 098502 (2006).
S2. T. Denk et al., Science **XXX**, XXXX (2009).
S3. R. N. Clark, P. G. Lucey , J. Geophys. Res. 89, 6341-6348 (1984).
S4. J. R. Spencer, L. A. Lebofsky, M. V. Sykes, *Icarus* **78**, 337-354 (1989).
S5. S. Albers. http://laps.noaa.gov/albers/sos/saturn/iapetus/iapetus_rgb_cyl_www.jpg (2008).
S6. D. E. Gault, F. Hoerz, D. E. Brownlee, J. B. Hartung 1974. *Proc. 5th Lunar Conf.***, 3**, 2365-2386 (1974).
S7. S. J. Ostro et al. Icarus 183, 479-490 (2006).
S8. G. J. Black, Campbell, D.B., Carter, L.M., Ostro, S.J., Science 304, 553 (2004).

www.sciencemag.org/cgi/content/full/1177088/DC1

Supporting Online Material for

Iapetus: Unique Surface Properties and a Global Color Dichotomy from Cassini Imaging

Tilmann Denk,* Gerhard Neukum, Thomas Roatsch, Carolyn C. Porco, Joseph A. Burns, Götz G. Galuba, Nico Schmedemann, Paul Helfenstein, Peter C. Thomas, Roland J. Wagner, Robert A. West

*To whom correspondence should be addressed. E-mail: Tilmann.Denk@fu-berlin.de

Published 10 December 2009 on *Science* Express
DOI: 10.1126/science.1177088

This PDF file includes:

Physical and Astronomical Properties of Iapetus

Equatorial diameter:	1491 km	(*S1*)
Polar diameter:	1424 km	(*S1*)
Flattening:	0.045	
Equatorial circumference:	~4700 km or ~13 km/deg.	
Surface area:	$6.7 \cdot 10^6$ km^2	
Volume:	$1.7 \cdot 10^9$ km^3	
Mass:	$1.806 \cdot 10^{21}$ kg	(*S2*)
Mean density:	1083 kg/m^3	(*S3*)
Mean surface gravity:	0.223 m/s^2	(*S3*)
Escape velocity:	580 m/s	
Semi-major axis:	3,560,851 km	(*S4*)
Siderial orbit period:	1904 h = 79.33 d	(*S4*)
Mean orbit velocity:	3.26 km/s	
Orbit excentricity:	0.0293	(*S4*)
Orbit inclination:	8.3° to local Laplace plane (which is inclined by 15.2° to Saturn's equator)	(*S4*)
Orbit precession period:	~3445 yrs	(*S4*)

Table S1. Physical and astronomical properties of Saturn's moon Iapetus

Cassini Observation Campaigns of Iapetus

Date	Orbit	Visible hemispheres	No. of requests	Pixel scales	Phase angles
Jul-Aug 2004	000	southern leading; trailing	9	15 - 54 km/pxl	54° - 112°
Oct 2004	00A	southern anti-Saturn; sub-Saturn*	11	6.7 - 19 km/pxl	47° - 161°
31Dec04-01Jan05	00B-00C	northern leading; northern sub-Saturn*	10	0.7 - 1.1 km/pxl	50° - 140°
Mar 2005	004-005	sub-Saturn/ leading	16	8.0 - 15 km/pxl	52° - 129°
Nov 2005	017-018	leading/ northern sub-Saturn	26	2.5 - 13 km/pxl	35° - 158°
Jan 2006	020	sub-Saturn	8	5.3 - 12 km/pxl	52° - 151°
Mar-Apr 2006	022-023	southern leading/ anti-Saturn	29	3.6 - 14 km/pxl	64° - 148°
Jun 2006	025	sub-Saturn	9	8.1 - 13 km/pxl	10° - 87°
Sep 2006	028	sub-Saturn	3	20 km/pxl	0° - 3°
Feb 2007	039	sub-Saturn	6	14 - 15 km/pxl	2° - 23°
Apr/Jun 2007	043, 047	sub-Saturn/ trailing	6	13 - 16 km/pxl	16° - 66°
Sep 2007	049-050	anti-Saturn/ trailing; sub-Saturn high-latitudes*	17	0.01 - 9 km/pxl	13° - 152°

Table S2. Major Cassini Iapetus observation campaigns during the primary mission (July 2004 - June 2008). The number of requests indicates the number of different observation perspectives during a campaign. The pixel scale indicates the spatial resolution of the Narrow-angle camera (NAC) images of the Cassini Imaging experiment (ISS). The best pixel scale of Iapetus images taken by the Voyager-2 spacecraft in Aug 1981 was 9 km/pxl.
*...in "Saturn-shine"

Determination of the Model Ages of the Young Bright Craters Within the Highest-resolution Images of Iapetus

The age calculations for small bright craters within Cassini Regio in Fig. 3C are first-order estimates and were determined as follows. In the highest-resolution images of the targeted Iapetus flyby on 10 September 2007 at 10-12 m/pxl (IDs: N1568126885 to N1568127660), 237 craters with diameters up to 200 m were identified within an area of ~500 km^2 showing brighter-than-average features, ranging from subtly lightened rims (~1.14x brighter than their environs) to obvious bright-floors and rims, and bright-ray systems about 4x brighter than the dark surroundings (crater Escremiz at 1.6°N, 173.5°W, diameter ~60 m is the most prominent). For each of these craters, the relative albedo of the bright feature was measured compared to an average dark part of the surface very close to the crater; this should generally compensate for different illumination conditions (phase angles of ~30° to ~70° in different images, varying incidence and emission angles due to surface topography). Using these measurements we have ordered these 237 craters in brightness. We assume that this order is inversely correlated to the crater age. This is a rough assumption, but should be sufficient for our purpose here.

This population of craters, apparently the most recent, can be given a very approximate age (accumulation time) from different models of impactor populations, fluxes, and sources. The model of Neukum (*S5*) gives (521 +110/-120) Ma, the model A of Zahnle (*S6*) gives (284 +92/-86) Ma, the model B of Zahnle gives (75 +25/-23) Ma. This would then be the time for brightest fresh-ice material to fade to ~1.14x of the background albedo.

Removing the brightest crater and calculating the model age again gives the model age of the surface in the past at the time just before the removed crater has been formed. Subtracting this age from the model age of all 237 craters results in an age estimate for the "removed" crater. This step can in principle be repeated for all craters.

However, in practice, a caveat is that the resolution limit of the images does not allow a direct determination of model ages for craters smaller than ~70 m. This is the reason why some data points in Fig. 3C are located vertically above their neighbors. Especially the brightest identified craters, like Escremiz, are mainly smaller than 70 m. Therefore, a power function is fitted to the calculated ages, shown as a line in the diagram. This power function is used to estimate the first-order ages given in the paper. Because of the many uncertainties of this rough estimation, only one significant digit is given.

This calculation is independent of the physical processes responsible for the fading.

References and Notes

S1. Most recent values for the Iapetus dimensions are provided by one of the co-authors (PCT).

S2. R. A. Jacobson *et al.*, presented at the "Saturn After Cassini-Huygens Symposium" held at Imperial College London, UK (2008).

S3. P. C. Thomas *et al.*, *Icarus* **190**, 573-584 (2007).

S4. http://ssd.jpl.nasa.gov/?sat_elem; Jacobson, R.A. (2009) SAT317 - JPL satellite ephemeris.

S5. G. Neukum, B. A. Ivanov, in *Hazards due to Comets & Asteroids*, T. Gehrels, Ed. (Univ. Arizona Press, 1994), pp. 359-416.

S6. K. J. Zahnle, P. Schenk, H. Levison, L. Dones, *Icarus* **163**, 263-289 (2003).

S7. T. Roatsch *et al.*, *Plan. Spa. Sci.* **57**, 83-92 (2009).

S8. We acknowledge the individuals at CICLOPS (at the Space Science Institute in Boulder, CO) and JPL (Pasadena, CA), as well as the members and associates of the Imaging Team for the successful conduct of the ISS experiment onboard the Cassini spacecraft. This paper is dedicated to Steve Ostro, whose work helped considerably to understand the nature of Iapetus' dark terrain. This work has been funded by the German Aerospace Center (DLR) and NASA/Jet Propulsion Laboratory.

Iapetus Cassini ISS Image Examples, and a Sketch Map Illustrating the Global Albedo and Color Dichotomies

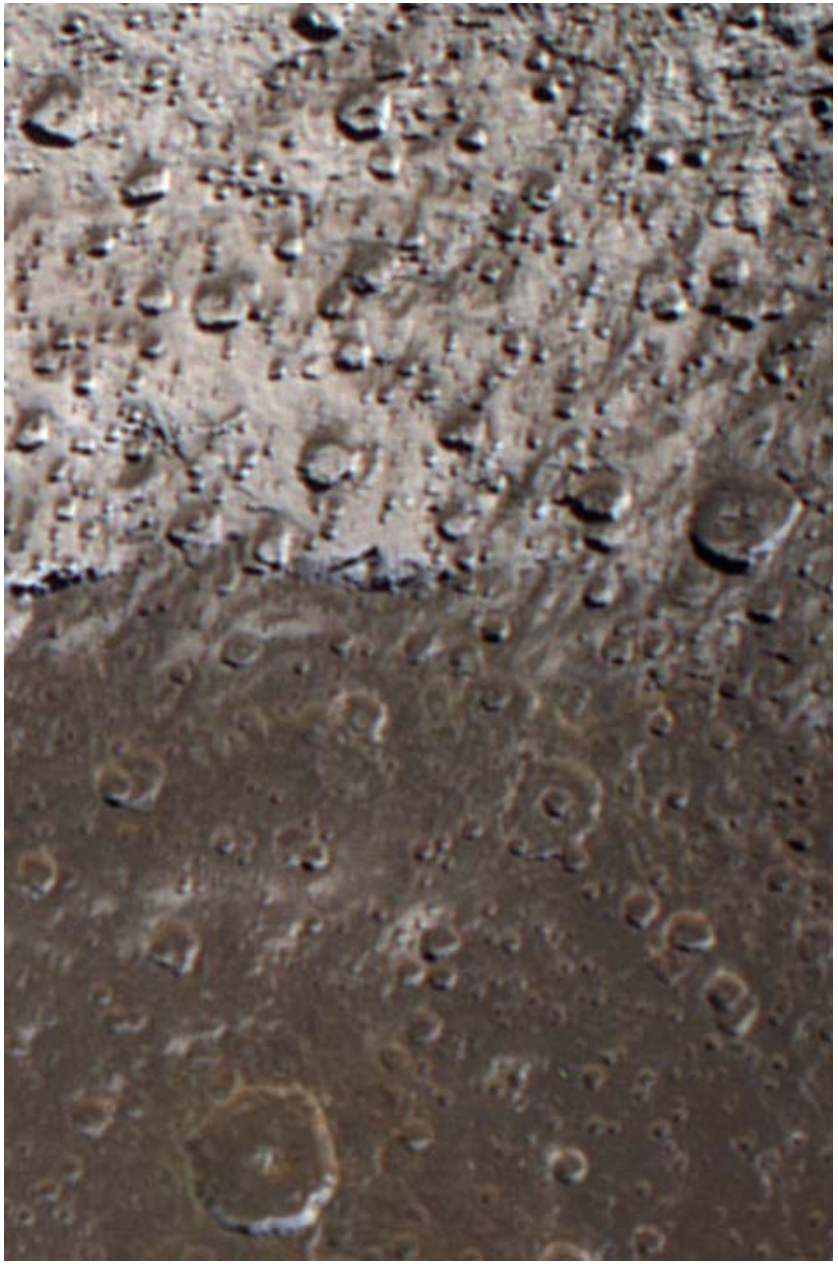

Fig. S1. Craters at the northern boundary of Cassini Regio on the leading side, observed during the B/C flyby on 31 Dec 2004; north is approximately up. Within the dark terrain, bright crater walls face the pole, whereas within the bright terrain, dark crater walls face towards the equator. The sun illuminates the scenery from the lower left, with black areas being shadows. Image IDs: N1483152058, N1483152093, N1483152170; pixel scale 1.03 km/pxl; the larger crater near the bottom of the image is Dapamort (37°N, 85°W, Ø 49 km).

Fig. S2. Dark-floor craters near the equator on Iapetus' trailing side, observed during the targeted flyby on 10 Sep 2007; north is up. Hamon (11°N, 270°W, Ø 96 km) is the large crater at middle right, Samson (7°N, 299°W, Ø 33 km) is at lower left. Located immediately north-east of Samson is an ~100 km long trough which also contains a dark floor. Image IDs: N1568157586 to N1568157685 and N1568159589 to N1568159640.

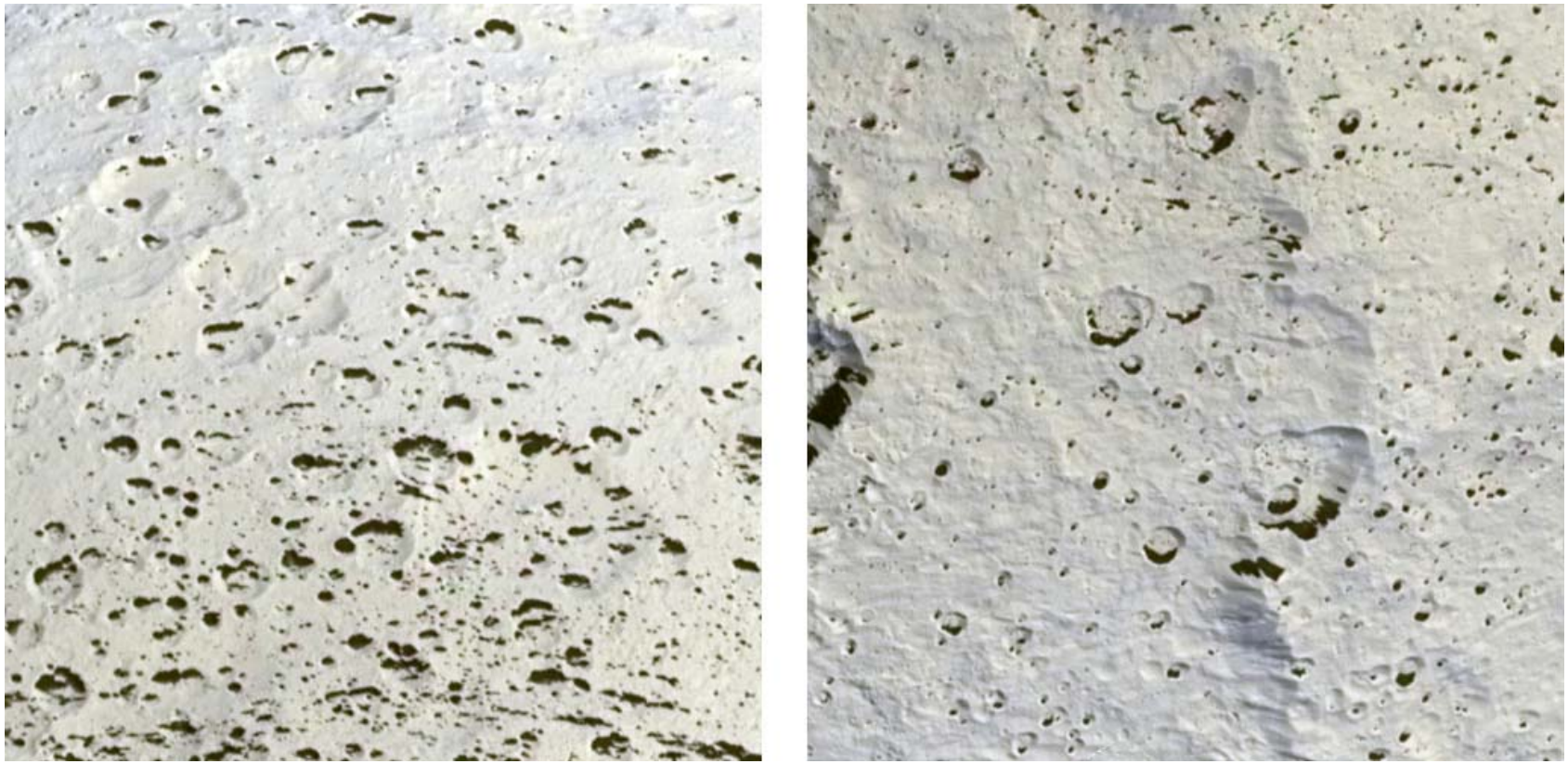

Fig. S3. Dark, equatorward-facing crater walls within the bright terrain on the trailing hemisphere, observed during the targeted flyby on 10 Sep 2007. North is up, the images' horizontal edge lengths are ~230 km.

Left: Northern hemisphere, the dark crater walls face southward, towards the equator (image center: ~40°N, 235°W; image IDs: N1568159089 to N1568159313).

Right: Southern hemisphere, the dark walls face toward north, also equatorward. The large north-south trending wall is the eastern edge of basin Gerin (46°S, 233°W, Ø 445 km; image IDs: N1568158122 to N1568158329).

Fig. S4. Parts of the eastern (*right*) and western boundary (*next page*) of the albedo dichotomy. The complex appearance of the dark/ bright pattern is not consistent with a formation by infalling material.

Right: Craters Naimon (9°N, 329°W, Ø 244 km) and Astor (15°N, 321°W, Ø 122 km), observed during the B/C flyby on 01 Jan 2005. North is approximately up; image ID: N1483247183. The image has been taken in Saturn-shine with an exposure time of 82 s while the spacecraft tracked Iapetus; the streaks outside Iapetus are smeared star trails.

Next page: Image mosaic of the equatorial transition terrain at ~220°W, observed during the targeted flyby on 10 Sep 2007. The large crater right of the image center is Eudropin (1°N, 221°W, Ø 42 km). North is up; image IDs: N1568133116 to N1568136601.

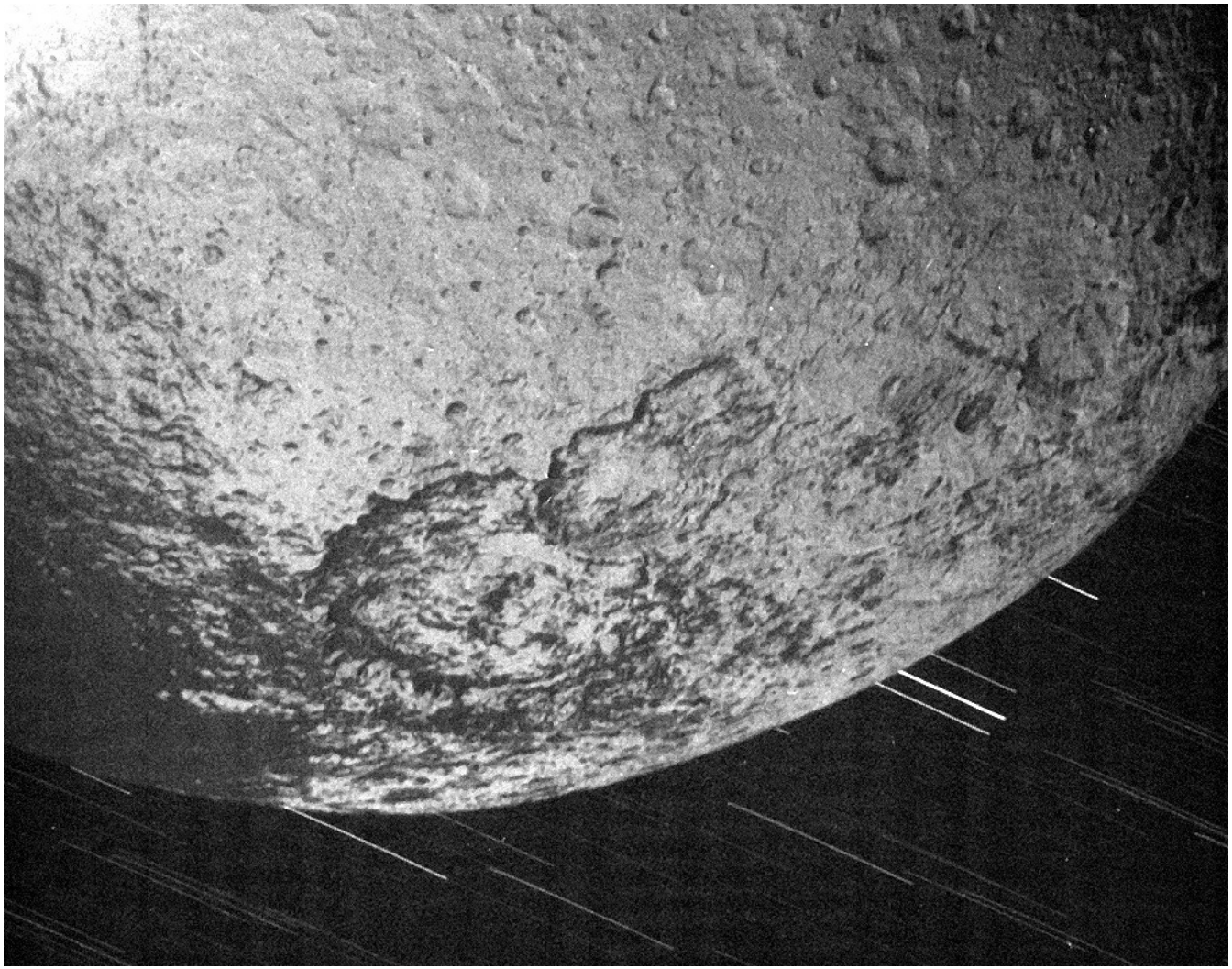

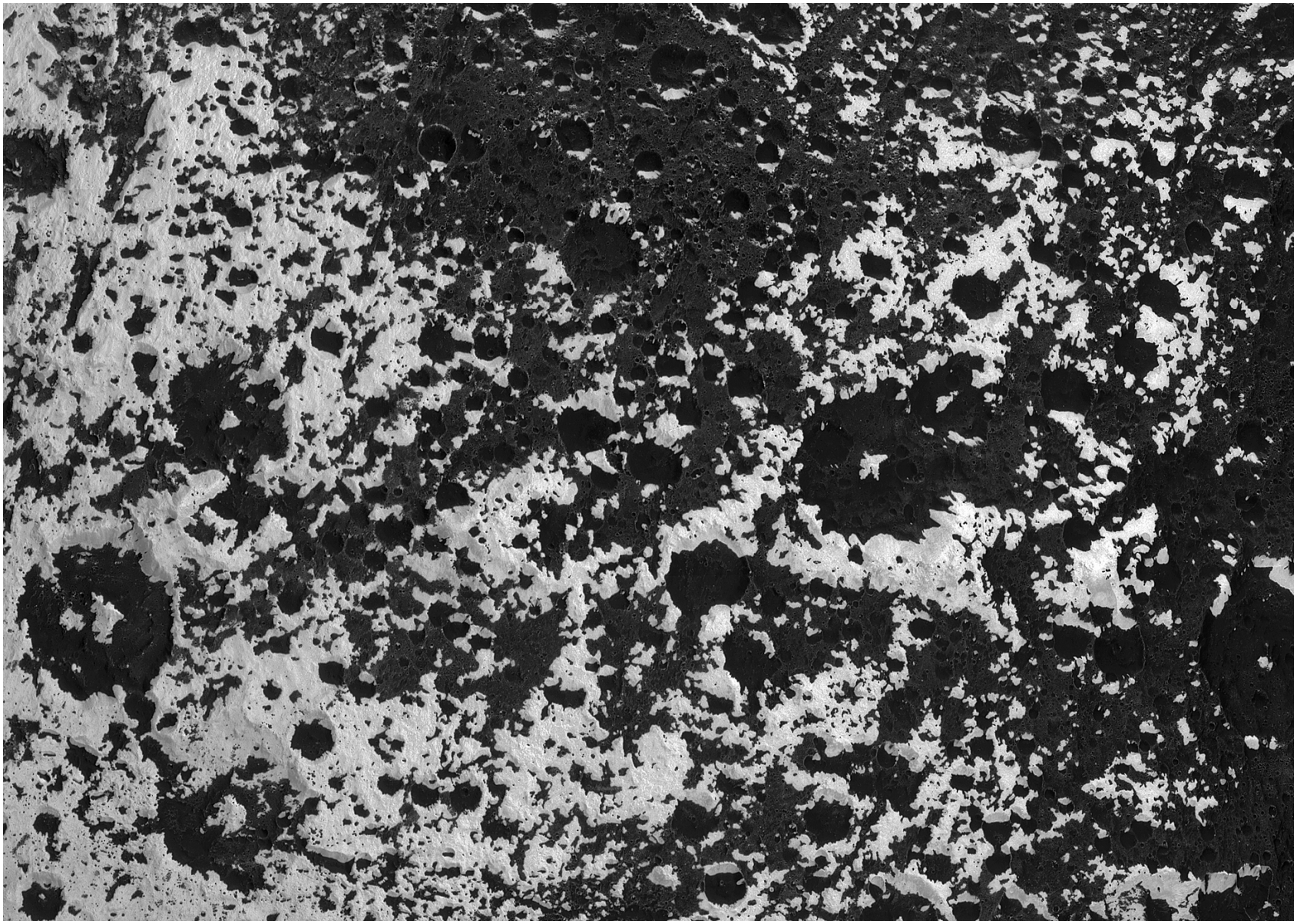

Fig. S4 *(cont.)*

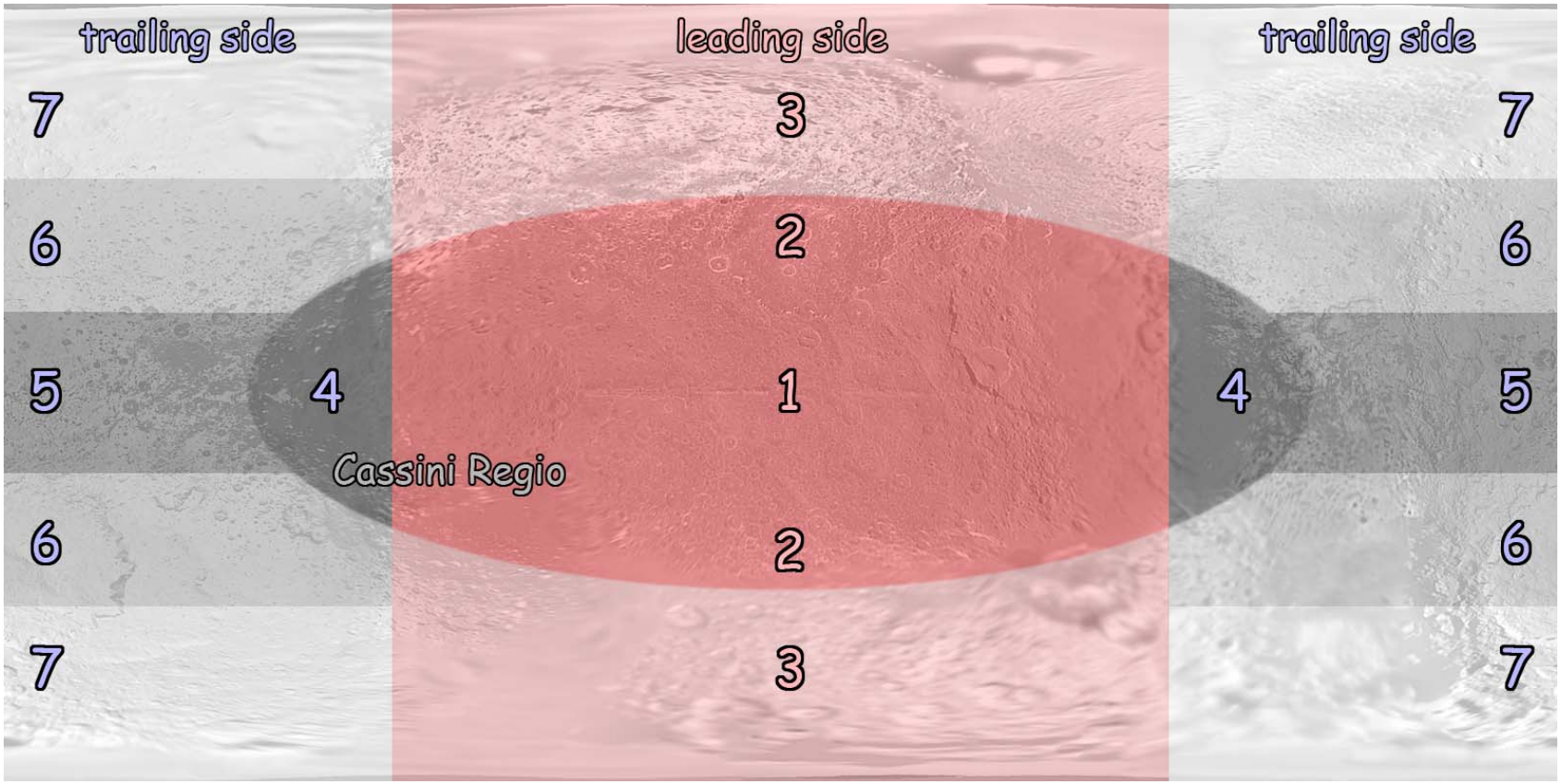

Fig. S5. Sketch map of global brightness and color variations on Iapetus, centered on the leading side (93°W).

1: central Cassini Regio, homogeneously dark, almost no bright patches, reddish color (see also Fig. S6);

2: mid-latitude portions of Cassini Regio, with bright crater walls facing poleward (cf. Fig. S1);

3: bright reddish high-latitude terrain on the leading side with dark crater walls facing equatorward (cf. Fig. S1);

4: parts of Cassini Regio extending onto the trailing side, showing a less reddish color (cf. Fig. S6);

5: equatorial part of the trailing side with a patchy distribution of bright and dark material even around the trailing side's center (cf. Fig. S2, S4);

6: low- to mid-latitude bright terrain with dark crater walls facing equatorward (cf. Fig. S3);

7: mid to high latitudes on the trailing side with "polar caps" and no exposed dark material.

The Iapetus basemap is from (*S7*).

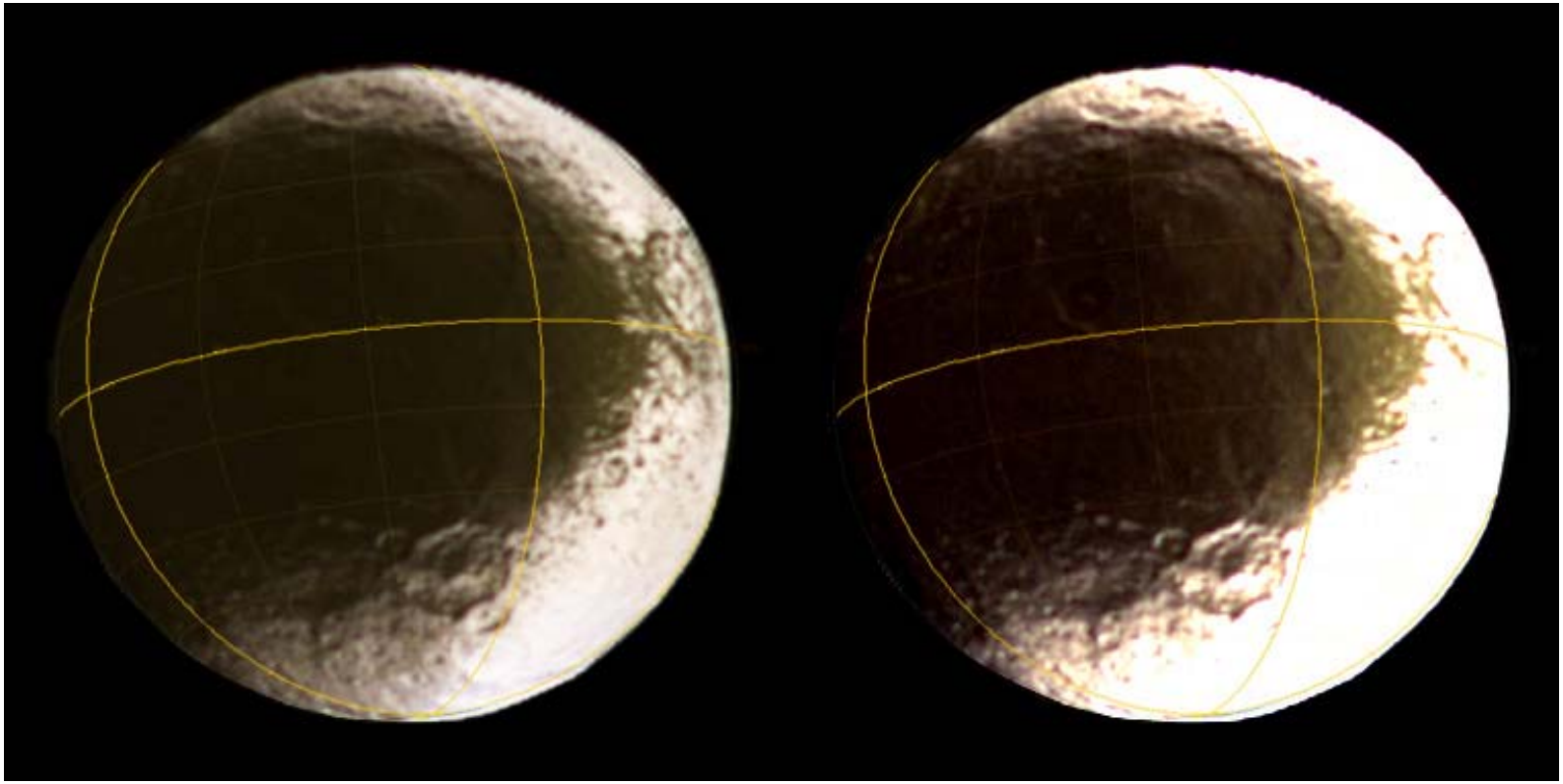

Fig. S6. Boundary of the color dichotomy on the sub-Saturn hemisphere near the 0°W meridian. *Left:* slightly contrast enhanced to show the boundary within the bright terrain. *Right:* same image, strong contrast enhancement to show the color variation within dark Cassini Regio. Grid: highlighted are the 0°W meridian, the 90° meridian (very left), and the equator. Observation date: 25 Jun 2006; pixel scale: 8.8 km/pxl; phase angle: 10°; sub-spacecraft point: 12°S, 26°W; used color filters: IR1 (758 nm), GRN (563 nm), UV3 (340 nm); image IDs: N1529894666 to N1529894704.

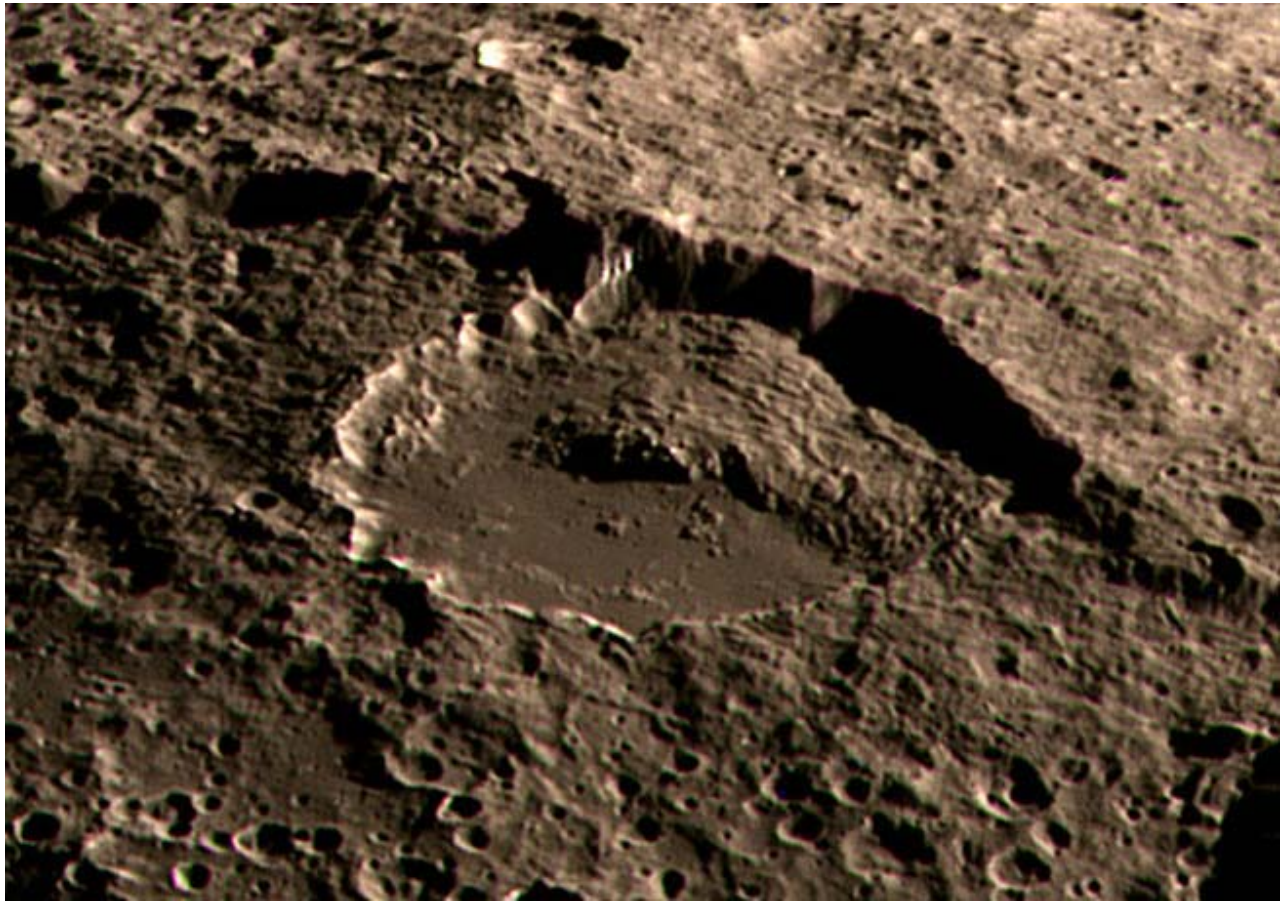

Fig. S7. Crater Malun (6°N, 41°W, Ø 121 km) has a very flat and almost crater-free floor and therefore is thought to be among the youngest large craters on Iapetus. Despite its relative youthfulness, its surface is completely dark, arguing for a darkening process that continued after Malun formed. Image IDs: N1483213275, N1483213337, N1483213455.

Comparison of Iapetus and Callisto

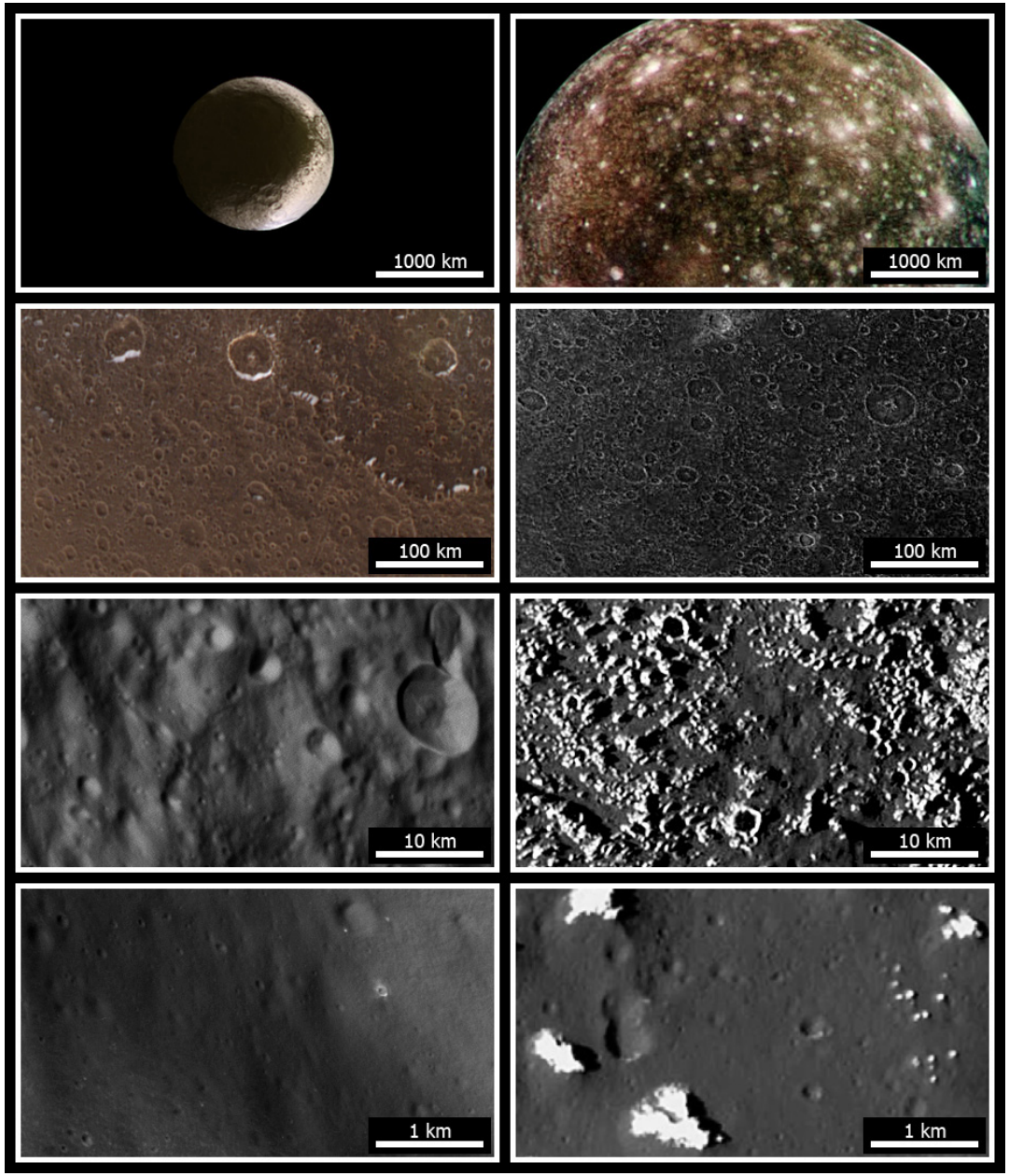

Fig. S8. Comparison of Iapetus dark terrain (Cassini ISS data, left) and the surface of Callisto (Galileo SSI data, right). The image pixel scales increase by a factor of 10 for each row. Due to insufficient data, the higher resolution images are not cutouts from the lower resolution data. All images are contrast-enhanced.

Top row (10 km/pxl): At global scales, Callisto appears generally dark, but mottled, while Iapetus shows the distinct albedo dichotomy with no obvious albedo variation within the dark terrain.

2nd row (1 km/pxl): At regional scales, Callisto craters show bright rims; a feature that Iapetus' craters only show at latitudes above ~28°.

3rd (100 m/pxl) and bottom (10 m/pxl) rows: At local scales, bright isolated hills, partly related to crater rims, are observed on Callisto but not on Iapetus deep within the dark terrain.

Data, from top to bottom (image IDs). Left column (Iapetus, Cassini ISS data): 1st: N1529894666 to N1529894704; 2nd: N1483152058, N1483152093, N1483152170; 3rd: W1568127660; 4th: N1568127660. Right column (Callisto, Galileo SSI data): 1st:30C0027 to 30C0029; 2nd: C3C0022; 3rd: 20C0002; 4th: 30C0007.